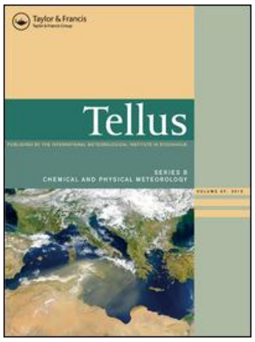

Tellus B: Chemical and Physical Meteorology

ISSN: (Print) 1600-0889 (Online) Journal homepage: http://www.tandfonline.com/loi/zelb20

Dust plume formation in the free troposphere and aerosol size distribution during the Saharan Mineral Dust Experiment in North Africa

Basit Khan, Georgiy Stenchikov, Bernadett Weinzierl, Stoitchko Kalenderski & Sergey Osipov

To cite this article: Basit Khan, Georgiy Stenchikov, Bernadett Weinzierl, Stoitchko Kalenderski & Sergey Osipov (2015) Dust plume formation in the free troposphere and aerosol size distribution during the Saharan Mineral Dust Experiment in North Africa, Tellus B: Chemical and Physical Meteorology, 67:1, 27170, DOI: 10.3402/tellusb.v67.27170

To link to this article: https://doi.org/10.3402/tellusb.v67.27170

Tellus
SERIES B
CHEMICAL
AND PHYSICAL
METEOROLOGY
PUBLISHED BY THE INTERNATIONAL METEOROLOGICAL INSTITUTE IN STOCKHOLM

Dust plume formation in the free troposphere and aerosol size distribution during the Saharan Mineral Dust Experiment in North Africa

By BASIT KHAN[1], GEORGIY STENCHIKOV[1]*, BERNADETT WEINZIERL[2], STOITCHKO KALENDERSKI[1] and SERGEY OSIPOV[1], [1]*King Abdullah University of Science and Technology, Thuwal, Saudi Arabia;* [2]*Deutsches Zentrum fur Luft- und Raumfahrt, Oberpfaffenhofen, Germany*

(Manuscript received 6 January 2015; in final form 31 October 2015)

ABSTRACT

Dust particles mixed in the free troposphere have longer lifetimes than airborne particles near the surface. Their cumulative radiative impact on earth's meteorological processes and climate might be significant despite their relatively small contribution to total dust abundance. One example is the elevated dust-laden Saharan Air Layer (SAL) over the tropical and subtropical North Atlantic, which cools the sea surface. To understand the formation mechanisms of a dust layer in the free troposphere, this study combines model simulations and dust observations collected during the first stage of the Saharan Mineral Dust Experiment (SAMUM-I), which sampled dust events that extended from Morocco to Portugal, and investigated the spatial distribution and the microphysical, optical, chemical, and radiative properties of Saharan mineral dust. The Weather Research Forecast model coupled with the Chemistry/Aerosol module (WRF-Chem) is employed to reproduce the meteorological environment and spatial and size distributions of dust. The model domain covers northwest Africa and adjacent water with 5 km horizontal grid spacing and 51 vertical layers. The experiments were run from 20 May to 9 June 2006, covering the period of the most intensive dust outbreaks. Comparisons of model results with available airborne and ground-based observations show that WRF-Chem reproduces observed meteorological fields as well as aerosol distribution across the entire region and along the airplane's tracks. Several mechanisms that cause aerosol entrainment into the free troposphere are evaluated and it is found that orographic lifting, and interaction of sea breeze with the continental outflow are key mechanisms that form a surface-detached aerosol plume over the ocean. The model dust emission scheme is tuned to simultaneously fit the observed total optical depth and the ratio of aerosol optical depths generated by fine and coarse dust modes. Comparisons of simulated dust size distributions with airplane and ground-based observations are good for optically important 0.4–0.7 μm particles, but suggest that more detailed treatment of microphysics in the model is required to capture the full-scale effect of large and very small aerosol particles beyond the above range.

Keywords: regional modelling, high resolution, WRF-Chem, SAL, boundary layer, dust load

1. Introduction

The Sahara desert is the largest dust source worldwide. It contributes more than half of the earth's mineral dust to the total global atmospheric dust budget (Prospero et al., 2002). Mineral dust particles from the Sahara often travel thousands of kilometres across the Atlantic Ocean and into Northern Europe (Prospero et al., 2002; Dinter et al., 2009). Dust uplifting has been the subject of multiple studies (Donnell et al., 2001; Takemi and Seino, 2005; Yasui et al., 2005). However, the quantity and size distributions of dust, as well as the relative importance of the meteorological processes triggering vertical transport over the Sahara, are not completely understood (Marsham et al., 2008; Laurent et al., 2010).

A variety of meteorological effects cause dust emissions over this region. They range in scale from synoptic to local and comprise disturbances from subtropical troughs, the Saharan Heat Low, Low Level Jets (LLJs), density currents (DCs), and dust devils. Interaction of multiscale

---

*Corresponding author.
email: georgiy.stenchikov@kaust.edu.sa

Citation: Tellus B 2015, **67**, 27170, http://dx.doi.org/10.3402/tellusb.v67.27170

subtropical disturbances with continental-to-local scale Saharan meteorological processes further complicates the picture (Donnell et al., 2001; Knippertz, 2008; Cuesta et al., 2009; Schepanski et al., 2009b; Solomos et al., 2012). On the synoptic scale, extratropical depressions and desert heat lows (Fiedler et al., 2014) are the most important phenomena related to southward penetrating upper-level troughs favourable to Harmattan wind development in winter and spring under meteorological conditions associated with intense anticyclone-genesis (Kalu, 1979; Knippertz and Fink, 2006; Knippertz et al., 2009a). On the mesoscale, DCs are important for dust mobilisation and transport (Reinfried et al., 2009; Emmel et al., 2010; Solomos et al., 2012). DCs can be triggered by downdrafts from convective storms, evaporative cooling, and orographic storm activity over mountains (Sutton, 1925; Knippertz et al., 2007). These systems can produce fast-moving 'dust walls' generally called 'haboobs' (Sutton, 1925; Membery, 1985; Knippertz et al., 2007). Night-time collapse of deep highly-turbulent desert boundary layer often causes development of strong nocturnal LLJs that are frequent at around 25°N within the study domain (Engelstaedter and Washington, 2007; Knippertz, 2008; Todd et al., 2008; Schepanski et al., 2009b). On the microscale, dust mobilisation is associated with dry convective mixing in the atmospheric boundary layer and wind-driven erosion from arid and semiarid topographical depressions (Gamo, 1996; Flamant et al., 2007). In addition, fast rotating dust devils and non-rotating convective plumes also contribute to dust emissions in this region (Koch and Renno, 2005). A comprehensive discussion of different meteorological mechanisms is given in the recently published book by Knippertz and Stuut (2014).

The SAMUM-I field campaign was conducted from 10 May to 7 June 2006 in Northwest Africa. The main aim of the campaign was to understand the microphysical and optical properties and the radiative effect of dust. Details of the SAMUM-I field experiment, instrumentation and data can be found in Heintzenberg (2008) and Weinzierl et al. (2009) as well as on the SAMUM website (www.samum.tropos.de/). The observation period is generally characterised by interactions between the West African Heat Low (HL), upper-level circulation in the subtropics, and the Intertropical Convergence Zone (ITCZ) (Knippertz, 2008). Convective cold pools and the breakdown of nocturnal LLJs are key regional-scale meteorological mechanisms responsible for dust emissions over northwestern Africa during summer (Heinold et al., 2013). Given the limited data from monitoring, the small number of field campaigns, and the complexity of the microphysical and radiative properties of atmospheric aerosols, regional dust modelling has been increasingly used to understand and investigate atmospheric aerosols and their associated meteorological effects (e.g. Cuesta et al., 2009; Solomos et al., 2012; Kalenderski et al., 2013; Prakash et al., 2015). High-resolution simulations reveal fine-scale meteorological and dust processes, which are otherwise not observed, and therefore facilitate an in-depth process analysis of emission, transport, deposition, radiative effects and size distribution of dust aerosols as well as meteorological mechanisms that trigger dust events in the northwestern Sahara (Zender et al., 2003a; Kalenderski et al., 2013; Prakash et al., 2015).

A number of regional modelling studies have been undertaken on the basis of the SAMUM-I campaign published in the *Tellus B* special issue in 2009. Heinold et al. (2009), for example, studied the spatial–temporal evolution of dust plumes and particle size distribution using a regional modelling system, Lokal Modell-Multi-Scale Chemistry Aerosol Transport (LM-MUSCAT). They conducted simulations at 28 km spatial resolution and, although large-scale meteorology was well matched with the model, their model tended to misrepresent moist convective events that Heinold et al. (2009) attributed to the deficiency of the employed Tiedke convective parameterisation. Laurent et al. (2010) studied the emission, distribution and physical properties of dust using essentially the same model, Consortium for Small Scale Modeling-MUSCAT (COSMO-MUSCAT), with improved description of dust emission, also with grid spacing of 28 km. This model simulated dust size distribution quite realistically; however, for some events the dust plumes were not correctly represented. Laurent et al. (2010) assumed that meteorological factors are responsible for the misrepresentation of dust load as well as vertical advection, and horizontal distribution of dust.

Reinfried et al. (2009) and Knippertz et al. (2009b) conducted high-resolution cloud-resolving simulations to quantify effects of DCs during the SAMUM-I campaign. Both studies simulated DCs and tested sensitivity to spatial resolution, model parameterisations of convection and microphysics.

The vertical structure of the aerosol layer during the SAMUM-I campaign was studied using ground-based Raman lidar and airborne high spectral resolution lidar aboard a Falcone airplane (Esselborn et al., 2009; Heinold et al., 2009; Tesche et al., 2009; Müller et al., 2012).

Kandler et al. (2009), Petzold et al. (2009), and Schladitz et al. (2009) conducted dust particle analysis during the SAMUM-I campaign to characterise the dust mineralogy, chemical composition, size distribution, optical properties and complex refractive index. They found that dust absorption is highly variable but single scattering albedo usually exceeds 0.96 for visible wavelength, which is higher than usually assumed in the model simulations. The complex part of the refractive index for dust-like particles is of the order of 0.004 for 0.55 μm wavelength and decreases to 0.0017 for 0.7 μm wavelength. The total mass concentrations of particles with $D > 0.5\,\mu m$ strongly depend on the wind speed, indicating the local production of large particles, which, for high wind situations, dominate the aerosol mass concentration.

In this study, an advanced meteorological regional model interactively coupled with an air quality module, WRF-Chem (Grell et al., 2005a), is used to conduct the process analysis for the SAMUM-I period. This model was not previously used by the SAMUM-I community and data from the SAMUM-I field campaign provide a great opportunity to evaluate model performance. Our research goals are as follows:

1. Calculate dust generation, vertical mixing and transport to the free troposphere accounting for fine-scale orographic effects, diurnal cycle of the Planetary Boundary Layer and land–sea interaction.
2. Study size distribution and radiative effect of the airborne mineral dust as it is represented by the WRF-Chem microphysical module, and test the WRF-Chem dust parameterisations.
3. Simulate dust outflow from the northwest African Coast to the Atlantic Ocean, its microphysical characteristics, interaction with the sea breeze, and formation of the aerosol plume detached from the ocean surface.

Some of the above issues, like dust generation during the SAMUM-I campaign, its optical effects, and vertical mixing, were addressed in the SAMUM special issue studies, but with coarser spatial resolution and using different modelling approaches. Thus, the present study shows the capability of WRF-Chem with 5-km grid spacing of capturing dust emission and transport processes during the SAMUM-I period. For other issues, like a free tropospheric plume formation over the ocean, the effect of breeze on the dust continental outflow, and the effect of diurnal variation of the boundary layer to the vertical mixing of dust to the free troposphere, the SAMUM-I database is used here for the first time.

The article is organised as follows. Section 2 describes methodology, available observations and model setup. Section 3 presents results. Section 4 provides a summary and conclusions.

2. Methodology

During the SAMUM-I campaign, horizontal and vertical dust plume structures were sampled (Weinzierl et al., 2009). Based on the dust loading and synoptic conditions over Morocco and northwest Africa, Knippertz et al. (2009a) divided the entire campaign period into three phases:

1. Dust phase 1 (DP-1) from 12 to 15 May 2006.
2. Dust phase 2 (DP-2) from 22 to 27 May 2006.
3. Dust phase 3 (DP-3) from 31 May to 7 June 2006.

The DP-2 and DP-3 phases are characterised by aerosols with high atmospheric optical depth, as dust was frequently mobilised by strong winds, dry convection, and DCs during these phases. Therefore the focus in this study is on the DP-2 and DP-3 periods.

2.1. Observations

A variety of satellite and ground-based observations are used to tune the model and evaluate the results of simulations. Upper-air and near-surface station observation data are obtained for the study period from the US National Climatic Data Center (NCDC) and University of Wyoming (UW, www.weather.uwyo.edu/upperair/sounding.html). A list of stations is presented in Table 1. The SAMUM-I airplane meteorological and dust observations are provided by the Deutsches Zentrum fur Luft und Raumfahrt (DLR) team, which conducted the field experiment.

Era-Interim (Era-I) reanalysis data produced by the European Center for Medium-Range Weather Forecasts (ECMWF) are also utilised to test the WRF-Chem model results. Era-I provides a comprehensive set of 3-hourly

Table 1. Description of stations used in the analysis

No	Station name	Code	Latitude	Longitude	Elevation (m, asl)	Data source
1	Rabat-Sale	RAB	34.050°N	6.767°W	79	NCDC
2	Casablanca	CASA	33.550°N	7.640°W	57	NCDC
3	Bechar	BEC	31.500°N	2.250°W	816	NCDC, UW
4	Ouarzazate	OZT	30.939°N	6.909°W	1140	NCDC, AERONET
5	Tindouf	TIN	27.700°N	8.160°W	439	NCDC
6	Zagora	ZGA	30.35°N	5.867°W	820	NCDC
7	In Salah	INS	27.230°N	2.500°E	269	NCDC, UW
8	Tamanrasset	TAM	22.780°N	5.510°E	1378	NCDC, UW, AERONET
9	Saada	SAD	31.626°N	8.156°W	420	AERONET
10	Ra-El-Ain	RAS	31.670°N	7.599°W	570	AERONET

surface parameters that capture the weather as well as land-surface conditions and 6-hourly upper-air parameters at 37 pressure levels up to 1 hPa on a $0.7^\circ \times 0.7^\circ$ latitude–longitude grid. Details of the dataset can be found in Dee et al. (2011) and on the ECMWF web page (www.apps.ecmwf.int/datasets/data/interim_full_daily/).

The spatial distribution of aerosol optical depth (AOD) is obtained from the Moderate Resolution Imaging Spectroradiometer (MODIS) instruments aboard the Terra and Aqua satellites. The MODIS instrument provides high radiometric sensitivity (12 bit) in 36 spectral bands ranging in wavelength from 0.4 to 14.5 µm. The spatial resolution varies between bands, with two bands at 0.25 km (at nadir views), five bands at 0.50 km, and the remaining 29 bands at 1.0 km. In this study, MODIS Level 2, Collection 5.1 granule data from the Terra and Aqua platforms are utilised. MODIS Level-2 data are derived from Level 1B and produced at a nominal spatial resolution of 10×10 km. AOD retrievals over land and sea derived from the dark target product (Remer et al., 2005, 2008) and the 'deep blue' product over bright land surfaces (Hsu et al., 2004) are used for comparison with the simulated optical properties of aerosols from WRF-Chem.

The observed AODs and retrieved aerosol size distributions are obtained from the ground-based remote sensing aerosol robotic network (AERONET) to validate the WRF-Chem aerosol output. AERONET sun photometers provide observations of spectral AOD on up to eight wavelength channels between 0.340 and 1.640 µm (Holben et al., 1998) and an angular distribution of sky radiance at four wavelengths (0.440, 0.675, 0.870, and 1.020 µm). The maximum AERONET uncertainty in AOD measurements is estimated to be 0.02 with the highest error in the ultraviolet wavelength (Holben et al., 1998; Eck et al., 1999). The calibrated sky radiance measurements typically have an uncertainty of less than 5% (Holben et al., 1998). The AOD data from AERONET are computed at three quality levels: level 1.0 (unscreened), level 1.5 (cloud screened) and level 2.0 (cloud screened and quality assured). We utilise primarily AERONET level 2.0 data but use level 1.5, when level 2.0 data are not available. Details of the AERONET data and instrumentation can be found in Holben et al. (1998), Holben et al. (2001), and on the AERONET website (www.aeronet.gsfc.nasa.gov/).

2.2. Experimental setup

2.2.1. Model. The regional meteorological Weather Research Forecast (WRF) model, developed by the National Center for Atmospheric Research (NCAR) USA, solves fully compressible, non-hydrostatic equations of atmospheric dynamics. The prognostic variables include three-dimensional wind vector (*u, v, w*), potential temperature, geopotential, surface pressure, turbulent kinetic energy, water vapour mixing ratio, and cloud water. The model uses a terrain-following, hydrostatic-pressure vertical coordinate system and horizontal numerical approximation is performed on the Arakawa C-grid (Grell et al., 2005a, 2005b; Skamarock et al., 2005). For advancing in time, the model uses second- and third-order Runge-Kutta time integration. WRF-Chem extends WRF to include a chemistry module fully coupled with meteorological processes. The module simulates dust emissions, transport, deposition, turbulent and convective mixing as well as atmospheric chemistry and aerosol microphysics (Grell et al., 2005a). In this study, WRF-Chem version 3.3.5 is used. It is configured with the Regional Acid Deposition Model 2 (RADM2) photochemical mechanism (Stockwell et al., 1990), the Jerome Fast photolysis scheme (Wild et al., 2000), and the Modal Aerosol Dynamics Model for Europe (MADE) and Secondary Organic Aerosol Model (SORGAM) (Ackermann et al., 1998; Schell et al., 2001). MADE/SORGAM uses the modal approach with three log-normally distributed modes (Aitken, accumulation, and coarse modes) to represent the aerosol size distribution. The aerosol species in MADE/SORGAM comprises sulphate, nitrate, ammonium, organic matter (OM), black carbon (BC), water, sea salt and mineral dust.

The following physical parameterisations are used to configure the model simulations: the Lin microphysics scheme; the Rapid Radiative Transfer Model (RRTM) both for longwave (LW) and shortwave (SW) radiation; the Mellor–Yamada–Janjic (MYJ) boundary layer scheme; the Noah land-surface model; and Grell cumulus parameterisation. We used the USGS land use and vegetation data (24 categories) to define the surface characteristics (Wang et al., 2014).

2.2.2. Model domain. To cover the entire observation area and account for processes that are responsible for the development of dust plumes during the entire experiment, the WRF-Chem model is run in the spatial domain from 14.62°N to 36.10°N in latitude and 15.0°W to 10.0°E in longitude with 5 km horizontal grid spacing (Fig. 1a). In the calculations, we used 550 grid points in the west–east direction and 484 grid points in the south–north direction, as well as 51 vertical levels with the top of the model domain at the 10 hPa level. The domain covers northwestern Africa including the southern Sahara, Morocco and adjacent waters (Fig. 1a). For a sensitivity study, we also run WRF-Chem with the identical settings but in a smaller domain from 10.5°W to 1°W in longitude and from 26°N to 36°N in latitude with 181×181 grid points (Fig. 1b) and

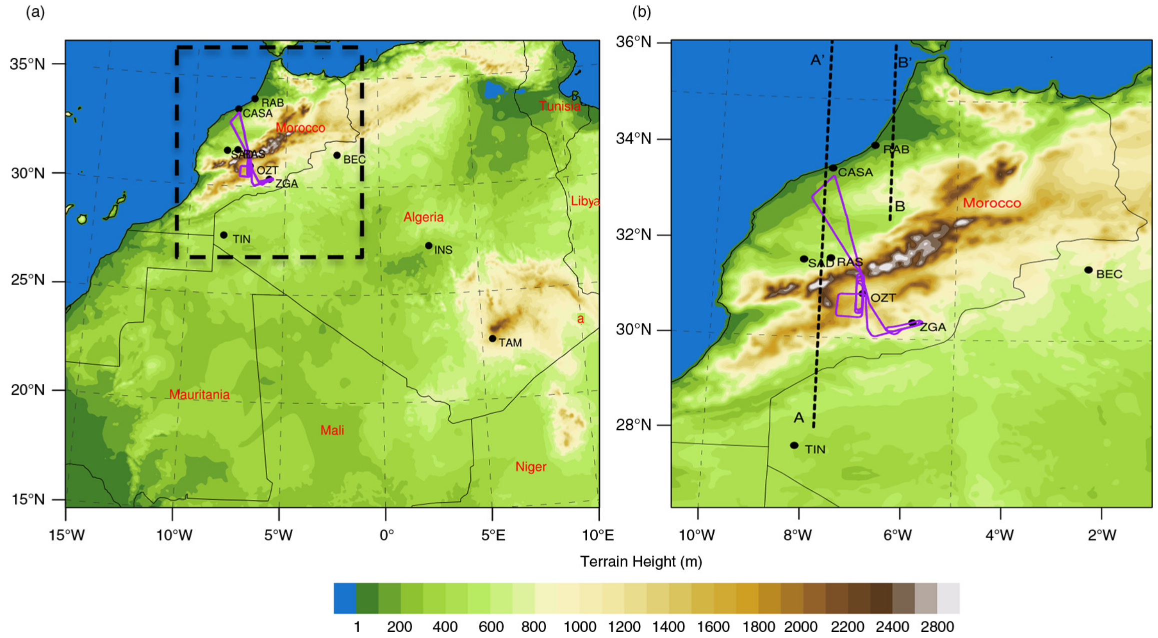

Fig. 1. Maps of the simulation domains with terrain height (shaded), SAMUM-I flight track (purple solid line) on 4 June 2006, and locations of observation stations used in the analysis: (a) the large domain with the black dashed box indicating the area of the small domain; (b) small domain; lines AA′ and BB′ show locations of vertical cross-sections at 7.79°W and 6.3°W, respectively. The description of the observation stations is provided in Table 1.

51 vertical levels. Below we refer to these domains as Large Domain (LD) and Small Domain (SD), respectively.

For successful simulations, the model domain should be large enough so that the meteorology is well reproduced, and all important dust sources are included. For example, when running simulations in SD, the model is able to reproduce meteorological processes but the simulated AOD is underestimated in comparison with AERONET observations. When running the simulation in LD the calculated AOD matches the AERONET AOD observations within the domain. Further increase of the domain does not affect the AOD significantly. Therefore production runs in this study are conducted in LD.

2.2.3. Initial and boundary conditions. The WRF-Chem model with the above settings is integrated for 21 d from 00:00 UTC on 20 May to 24:00 UTC on 9 June 2006 through most of the duration of the SAMUM-I experiment.

Lateral boundary and initial conditions for meteorological fields are provided by the National Centers for Environmental Prediction's (NCEP) global analysis (FNL) with a horizontal resolution of $1^\circ \times 1^\circ$. We use NCEP's daily global sea surface temperature (SST) analysis (RTG_SST_HR) to define the bottom boundary conditions over the ocean. Both lateral and bottom boundary conditions are updated every 6 hours.

Initial and boundary conditions for aerosol- and gas-phase species are taken from the default WRF-Chem profiles, which are obtained from various field studies to capture clean atmosphere, maritime, and mid-latitude conditions (McKeen et al., 2002). Anthropogenic emissions are provided by the REanalysis of the TROpospheric (RETRO) chemical composition inventories (www.retro-archive.iek.fz-juelich.de/) and by the Emission Database for Global Atmospheric Research (EDGAR) (www.edgar.jrc.ec.europa.eu). Biomass burning emissions are obtained from the Global Fire Emissions Database, Version 2 (GFEDv2.1) (Randerson et al., 2007) with a $1^\circ \times 1^\circ$ latitude–longitude spatial resolution and 8-d temporal resolution. All emission inventories are pre-processed by the PREP-CHEM-SRC v1 emissions pre-processor (Freitas et al., 2011). Biogenic emissions are not included in this study. We assume zero initial dust concentrations and no dust inflow through the lateral boundaries.

2.3. *Evaluation of model meteorology*

During the study period, northwestern Africa was affected by weather systems from the north. The meteorological analysis of this period was presented by Knippertz et al. (2009a). To evaluate the performance of WRF-Chem during the entire simulation period, we first compare the mean Era-I fields for the period from 22 May to 7 June

2006 with the WRF-Chem output for the same period. The correlation coefficient of 2 m temperatures (T_{2m}) in WRF-Chem and Era-I is greater than 0.97 with an RMSE of 1.57 K. The domain average time means (T_{2m}) are 28.0 and 29.0°C from WRF-Chem and Era-I, respectively, because of higher terrain and associated orographic cooling. T_{2m} in WRF-Chem is 1°C colder than in the lower resolution Era-I output. Over most of the Sahara, WRF-Chem is slightly colder than in Era-I, but the model overestimates T_{2m} in the northern foothills of the Atlas Mountain range and further north over the Moroccan plains. The distribution of wind at 10 m (U_{10m}) is consistent with the topographical features of the model domain. The correlation coefficient between WRF-Chem and Era-I surface winds is greater than 0.50 with an RMSE of ~ 1.39 m s^{-1}. The domain average time mean, WRF-Chem U_{10m}, is 1 m s^{-1} stronger (5.5 m s^{-1}) than that from Era-I. Over the flat desert, where most of the dust generation takes place, the mean wind difference between the model and Era-I, is 30% smaller than the domain average.

To evaluate how WRF-Chem performs on fine temporal and spatial scales, the meteorological characteristics from the WRF-Chem simulations are compared with those measured along the flight track of the research aircraft. During the SAMUM-I campaign, a DLR Falcon research aircraft was used for 17 research flights from 18 May to 7 June 2006. The durations of these flights varied from 37 minutes to more than 3 hours. Presented in Fig. 2 are the plots for the longest flight that took off on 4 June 2006. Figure 2 shows observed (red) and simulated (blue) wind speed, wind direction, air temperature and specific humidity along the flight track shown in Fig. 1b. The basic meteorological characteristics are reproduced more accurately at higher elevations where there is less meteorological noise from high-frequency boundary layer processes. The agreement for winds is not as good as that for temperature. The RMSE for wind speed is 2.89 m s^{-1}. The RMSE for both U and V components are 0.89 and 3.77 m s^{-1}, respectively. WRF-Chem generally overestimates water vapour at high elevations above 6 km (see Fig. 2d); at lower elevations, however, WRF-Chem shows better capability in predicting water vapour.

To further evaluate the simulated fields, we make comparisons with the available upper atmosphere soundings. The radiosonde data (air and dew point temperatures, and wind) at 1200 UTC on 4 June 2006 from three stations in the Sahara Atlas region (Tamanrasset, In Salah, and Bechar, see Table 1 and Fig. 1 for station locations) are obtained from University of Wyoming (Fig. 3). The stations are characterised by quite different meteorological conditions. The model performed exceptionally well for air temperature at three stations. At Tamanrasset (Fig. 3a) both simulated moisture (mixing ratio ~ 3.0 g kg^{-1}) and PBL height (~ 4.0 km asl) are in good agreement with observations. The model underestimated PBL height at the remaining two stations (Bechar and In Salah). The observations at In Salah (Fig. 3b) show a well-mixed layer in the first 2.0 km with a weak inversion above, however the PBL top with a capping inversion is around 4.0 km asl. The model underestimated both PBL height (~ 2.0 km) and moisture content (mixing ratio ~ 3.0 g kg^{-1}) at this station followed by a hydrolapse above. The observed mixing ratio within the PBL at In Salah is ~ 3.5 g kg^{-1}. At Bechar (Fig. 3c), the model simulated PBL is < 3.0 km while the observations show PBL top at 4.0 km asl. The model overestimated moisture (mixing ratio ~ 5.0 g kg^{-1}) within the PBL at Bechar. The simulated atmosphere reaches near saturation at around 2.7 km asl, although the observed atmosphere is quite dry at this level and does not give any indication of cloud condensation.

The strongest simulated and observed winds in the PBL are recorded at In Salah with the wind speed exceeding 12 m s^{-1} from the NE direction (Fig. 3b). The weakest PBL winds are recorded at Bechar (< 5 m s^{-1}) while at Tamanrasset, we see a moderate westerly flow of ~ 7 m s^{-1}. During the daytime, the northeasterly flow prevails. Wind speed at the top of the boundary layer reaches 15 m s^{-1} at Tamanrasset and Bechar (Fig. 3a and c), while a slightly weaker northerly wind of 12 m s^{-1} is recorded at In Salah (Fig. 3b). Surface winds are better captured by the model than higher up at all locations. The discrepancy does not exceed 1 m s^{-1}.

2.4. *Model dust generation and size distribution*

To calculate dust influx into the atmosphere, the Goddard Global Ozone Chemistry Aerosol Radiation and Transport (GOCART) dust emission scheme (Ginoux et al., 2001) is employed in WRF-Chem. GOCART scheme simulates dust emission as a function of the wind speed at 10 m altitude above the ground, U_{10m} (Chin et al., 2002). Emission dust mass flux, F_p, for a specific aerosol size group p is defined as:

$$F_p = \begin{cases} CSs_p(U_{10m}^2 - U_t) & \text{if } U_{10m} > U_t, \\ 0 & \text{otherwise} \end{cases} \tag{1}$$

where C is a dimensional constant coefficient that directly controls the magnitude of the dust emission flux; S is the dimensionless erodibility field taken from Ginoux et al. (2001) with a spatial latitude–longitude resolution of $0.25° \times 0.25°$; S accounts for soil susceptibility to wind stresses, surface roughness, and vegetation cover. U_t is the threshold velocity of wind erosion, which depends on particle size and surface wetness; and s_p is a particular particle size mass fraction injected in the atmosphere.

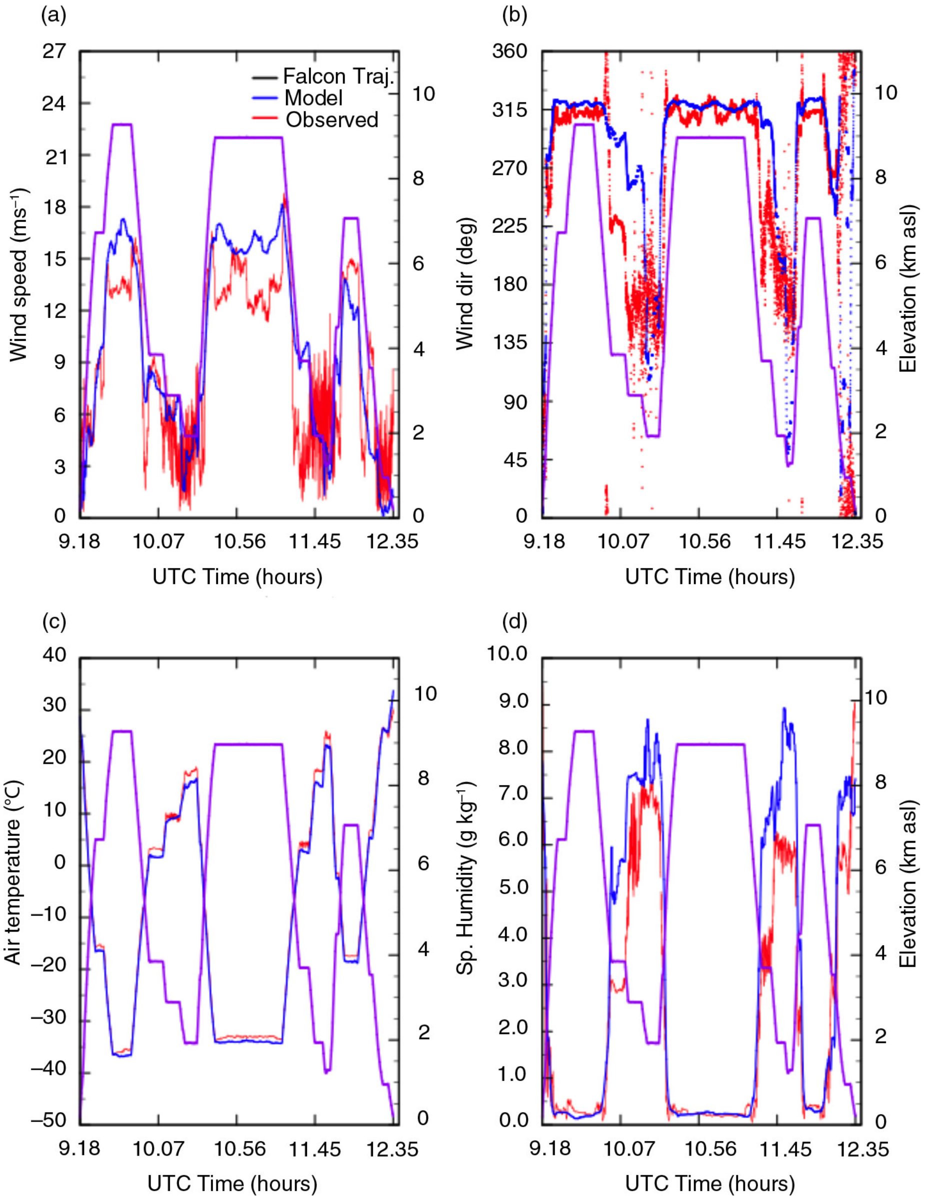

Fig. 2. Plots of the model (blue) wind speed (m s^{-1}), wind direction (degrees), air temperature (°C) and specific humidity (g kg^{-1}) with the aircraft observations (red) conducted during the research flight on 4 June 2006 from 09:18 to 12:35 UTC. The solid purple line shows the height of the flight trajectory (km) with respect to the vertical axis on the right.

Dust is a primary aerosol and does not have a nucleation Aitken mode, but comprises accumulation (or fine) and coarse modes. Therefore MADE/SORGAM approximates the dust size distribution using the two-mode log-normal size distributions to represent coarse and fine (accumulation) modes:

$$\frac{dN}{dD} = \frac{N_{fine}}{D \ln \sigma_{fine} \sqrt{2\pi}} e^{-\frac{\left(\ln(D)-\ln\left(D_{fine}\right)\right)^2}{2\ln^2 \sigma_{fine}}} + \frac{N_{coarse}}{D \ln \sigma_{coarse} \sqrt{2\pi}} e^{-\frac{(\ln(D)-\ln(D_{coarse}))^2}{2\ln^2 \sigma_{coarse}}} \quad (2)$$

where N_{fine} and N_{coarse} are total number concentrations, D_{fine} and D_{coarse} are modal diameters, and σ_{fine} and σ_{coarse} are the geometric standard deviations of fine and coarse modes, respectively. The MADE/SORGAM model predicts the spatial–temporal evolution of the modal diameter and number concentration for each mode; however, the geometric standard deviations for both modes are kept fixed:

$$\sigma_{fine} = 2 \text{ and } \sigma_{coarse} = 2.2 \quad (3)$$

The number and size distribution of dust particles entering the atmosphere from the surface in eq. (1) depend

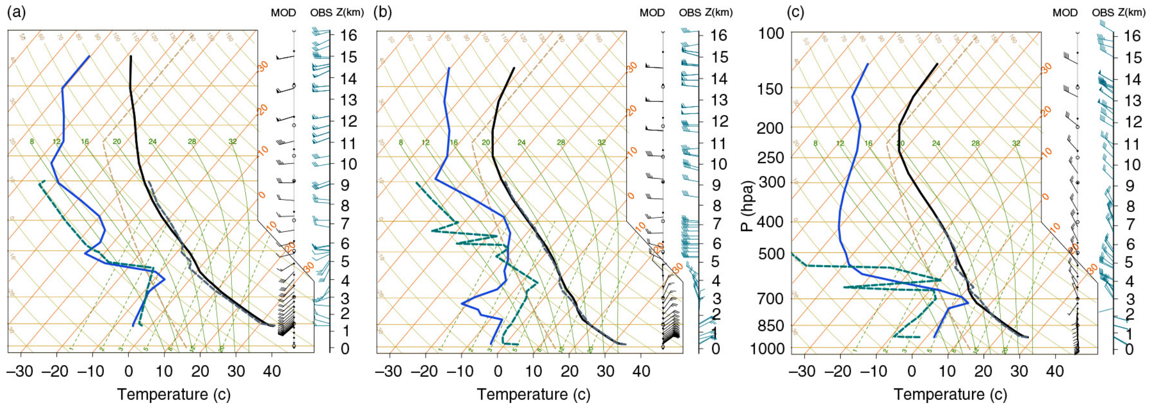

Fig. 3. Skew-T plots of simulated and observed soundings on 4th June 2006 for (a) Tamanrasset, (b) In Salah, and (c) Bechar at 12:00 UTC. Solid black and blue curves show air and dew point temperatures (°C) from the model while dashed grey and dashed cyan curves show observed soundings of air and dew point temperatures, respectively. Black wind barbs show model wind vector while cyan colour barbs show observed winds in knots.

on surface wind, as well as soil type and its physical conditions (Kok, 2011a, 2011b; Kok et al., 2012). The size of particles is especially important because it defines particle lifetime and affects aerosol optical properties. In the standard WRF-Chem setup, the emitted dust mass flux in eq. (1) is distributed in two modes (2), with fixed modal diameters of

$$D_{fine} = 0.6\,\mu\text{m and } D_{coarse} = 6\,\mu\text{m} \tag{4}$$

The mode mass fractions are

$$\begin{aligned} S_{fine} &= 0.07 \text{ and } S_{coarse} = 1 - S_{fine} \\ &= 0.93\left(S_p = 0 \text{ for Aitken mode}\right) \end{aligned} \tag{5}$$

The fixed geometric standard deviations σ_{fine} and σ_{coarse} are as in eq. (3). In the atmosphere, dust particles are advected by winds, mixed by turbulence, microphysically interact with aerosols and water, experience chemical transformations, and deposit, forming an airborne aerosol particle distribution that is different from that coming from the surface (Zender et al., 2003b; Shao, 2008). To estimate uncertainties in aerosol microphysical models, Zhao et al. (2013) conducted WRF-Chem simulations with tuned meteorology using bin Model for Simulating Aerosol Interactions and Chemistry (MOSAIC) and modal MADE/SORGAM microphysical dust size parameterisations. They found that the different microphysical models could result in significant differences in aerosol size distribution. Thus, model predictions have to be reconciled with available observations.

2.5. *Dust emission tuning*

The dust generation process is very complex. None of the available approaches are able to describe it from the first principles. The GOCART scheme (1) is one of the simplest among the known dust generation parameterisations (Marticorena and Bergametti, 1995; Shao, 2001, 2004, 2008; Zender et al., 2003b). However, it is fast and does not require diverse input information as most of the complexity of dust emission process is absorbed by an empirical source function *S*. This simple approach was chosen for the present study but adjusted for the specific conditions of the SAMUM-I case study to match the available observations. In this study, the GOCART parameterisation (1) is tuned to simultaneously match the observed optical depth and dust size distribution constraints from AERONET.

The coefficient *C* in eq. (1) was originally estimated to be equal to 1 mg s^2 m^{-5} based on regional datasets (Ginoux et al., 2001). Zhao et al. (2010) proposed tuning this parameter to replicate the consistency of the calculated optical depth with AERONET observations.

Figure 4 compares simulated AOD from the run in LD (blue solid line) with that from four AERONET sites (red dots) within the SAMUM-I region: Ouarzazate, Ras-El-Ain, Saada, and Tamanrasset (see Fig. 1). The simulations were conducted with the default s_p values (5) and empirical constant $C = 0.65\,\text{mg}\,\text{s}^2\,\text{m}^{-5}$, which was suggested by Zhao et al. (2010). The simulated AOD reproduces the magnitude and temporal evolution of observed AOD at all four AERONET sites quite reasonably. So varying total emissions can be matched to the observed optical depth, but cannot constrain the dust size distribution.

However, life time and radiative effects of dust particles are critically dependent on particle size and composition (Sokolik and Toon, 1999; Dubovik et al., 2006). The size range of particle radii spreads across two orders of magnitude, roughly from 0.1 to 10 microns and the Mie solution predicts that the extinction efficiencies of individual coarse-to-fine particles range across four orders of

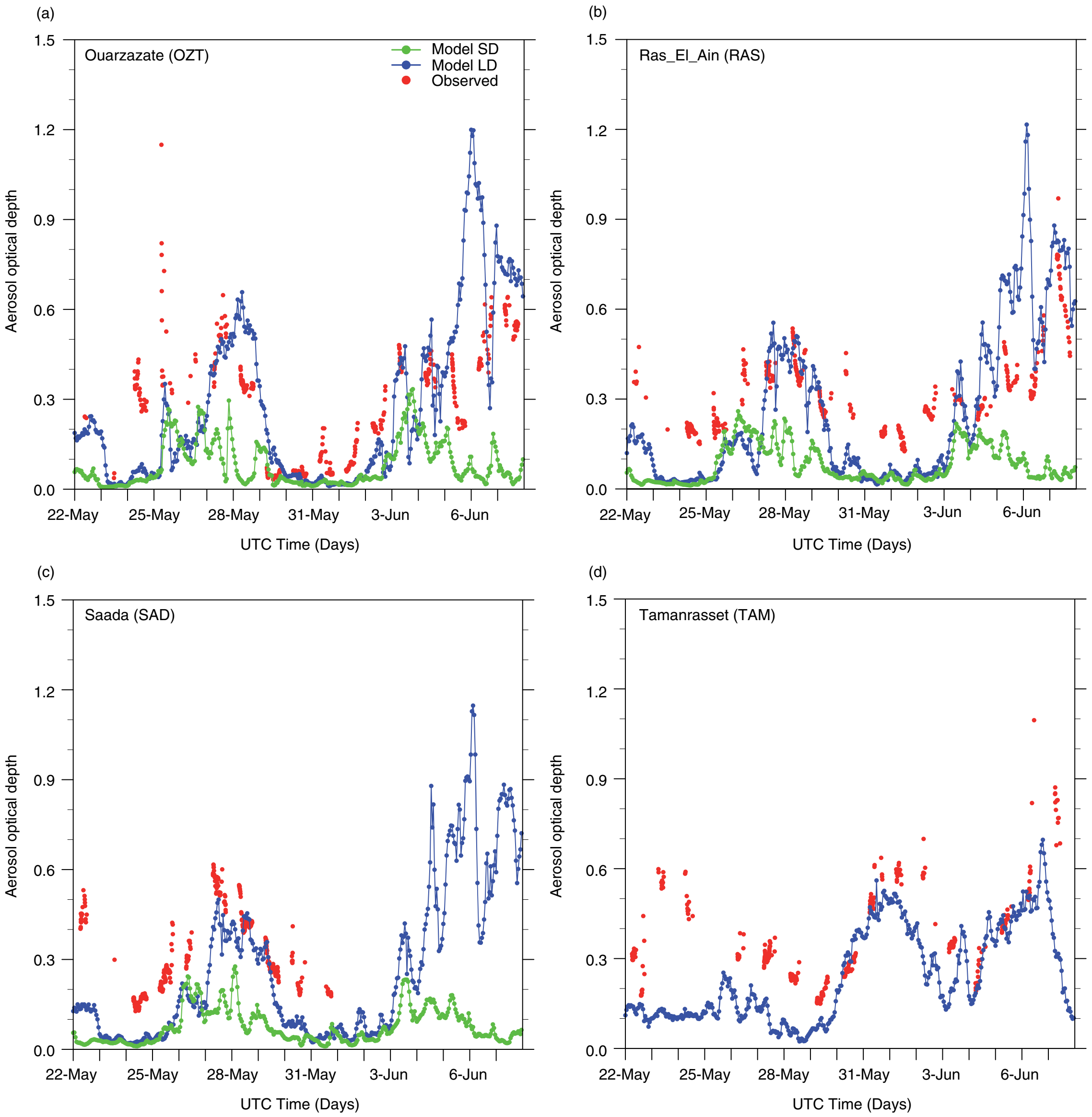

Fig. 4. Plots of the column AOD time series for the period of the SAMUM-I experiment: observation at 0.551 μm (red) from four AERONET stations and simulation at 0.6 μm in the LD (blue) and SD (green) at (a) Ouarzazate (OZT), (b) Ras-Al-Ain (RAS), (c) Saada (SAD), and (d) Tamanrasset (TAM). The geographical coordinates of the AERONET stations are provided in Table 1. AERONET level 1.5 data are used. TAM is beyond SD, and therefore TAM AERONET AOD cannot be compared with the AOD simulated in SD.

magnitude, because efficiencies are proportional to squared particle radii. Nevertheless, small particles are optically more efficient per unit mass because the number of particles is inversely proportional to the cubed particle radius. Large particles have shorter lifetimes in the atmosphere because of their higher deposition velocities. However, based on the measurements conducted during the ACE-2 campaign of 1997, Otto et al. (2007) found that the contribution of coarse particles in atmospheric heating rates and their effect on the top of the atmosphere and surface radiation balances prevails over those of fine particles. Weinzierl et al. (2009) confirmed this observation for SAMUM-I.

WRF-Chem with the default mode mass fraction s_p and $C = 0.65\,\mathrm{mg\,s^2\,m^{-5}}$ incorrectly represents contributions of the fine and coarse modes in the total optical depth. The model overestimates the optical depth of the fine mode and underestimates the optical depth of the coarse mode (not shown) in comparison with the AERONET Spectral Deconvolution Algorithm (SDA) Level 2.0 retrieval available at one AERONET station at Ouarzazate. SDA provides column-integrated optical depth for the coarse

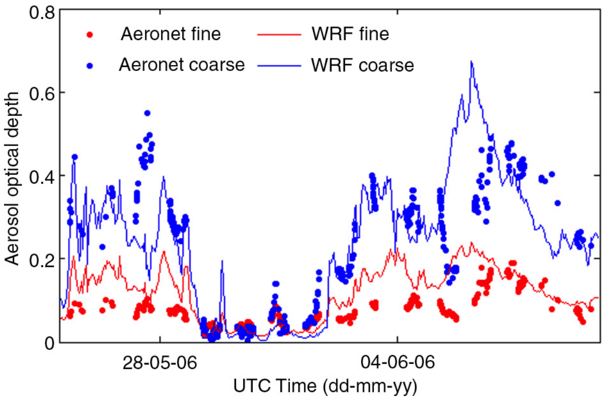

Fig. 5. Plots of the column AOD time series for 0.6 μm from the WRF-Chem simulations (solid lines) and AERONET observations for 0.551 μm (filled circles) for the fine (red) and coarse (blue) modes at the location of the Ouarzazate AERONET station. The AERONET retrievals are calculated using the Spectral Deconvolution Algorithm (SDA).

and fine modes separately, showing that in observations the optical depth of the coarse mode exceeds that of the fine mode (see Fig. 5), in agreement with the findings of Ryder et al. (2013) and Otto et al. (2007). To overcome this deficiency and to reproduce the observed contributions of coarse and fine modes in the simulations, in eq. (1) the mass fraction for a fine mode is decreased by a factor of seven, redirecting the residual mass into a coarse mode, and C is slightly increased to keep the total optical depth as in the AERONET observations. Kok (2011b), consistent with our findings, mentioned that the current parameterisations overestimate the fine mode emission flux by an order of magnitude. With the modified model settings:

$$S_{fine} = 0.01;\ S_{coarse} = 0.99;\ C = 0.75 \times 10^{-9}\,\mathrm{kg}\,s^{-2}m^{-5}, \quad (6)$$

the model results are in qualitative and quantitative agreement with AERONET observations (Fig. 5). In Fig. 5, the coarse mode optical depth (blue) in both simulations and observations is twice as large compared with the fine mode optical depth (red). The simulated (solid line) and observed (filled circles) AODs are in good agreement for the entire period of simulations. All results presented below are obtained using settings from eq. (6).

3. Results

3.1. *Dust sources activated during the SAMUM-I simulation period*

From 22 May to 7 June 2006, six main emission areas are activated (Schepanski et al., 2009a; Laurent et al., 2010; Ashpole and Washington, 2013a, Ashpole and Washington, 2013b). They are shown in Fig. 6 (areas *A, B, C, D, E, F*), which depicts average dust emissions for the entire period from WRF-Chem simulations. The colour shading indicates the average rate of dust emission.

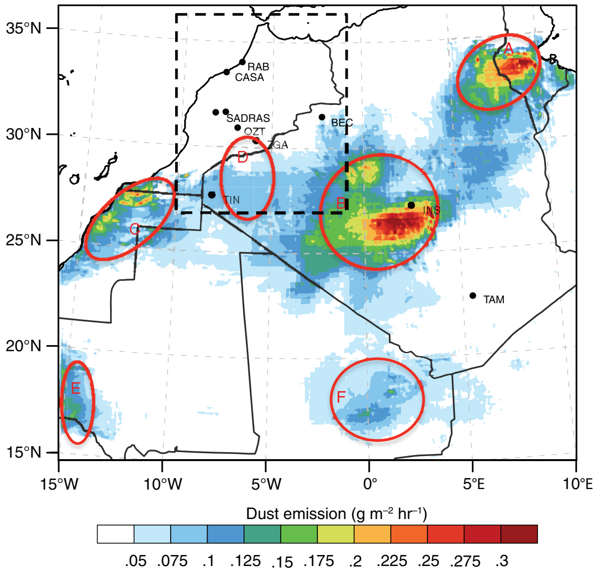

Fig. 6. Spatial distribution of time average dust emissions (shaded) in g m^{-2} h^{-1} from 22 May to 7 June 2006. The coloured circles marked as A, B, C, D, E and F show emission areas of Chotts Aljarid, Grand Erg Occidental, western Sahara, haboob activity area near Tindouf, the Senegal River basin, and the upper Niger River basin, respectively. The black dashed line box shows the small domain area.

Area *A* is the region of Chotts. It comprises a large area of ephemeral lakes that stretches from the lowlands of Tunisia to the Atlas Mountains of northern Algeria and is a well-known dust source region (Prospero et al., 2002; Mahowald et al., 2003; Schepanski et al., 2009b; Ginoux et al., 2012). The Chotts area is in the rain shadow of the Algerian Atlas Mountains. Precipitation in the Chotts area is less than 100 mm per year. According to Prospero et al. (2002), the most intensive dust emission occurs in an area centred at 7.5°E, 33.5°N during April–May and it could extend to August–September. The model captures significant dust emissions from this area on 24, 25, 26, 30 May, and 1 June. The strong wind gusts that lead to emissions in the Chotts area can be attributed to lee cyclones that develop to the south of the Atlas Mountain range (Knippertz et al., 2009a).

Area *B* is the topographical low region of Grand Erg Occidental located to the west of the Ahaggar Mountains comprising hydro (ephemeral lakes) and non-hydro natural dust sources (Ginoux et al., 2012). These lakes formed because of weathering and runoff from the mountains (Prospero et al., 2002). Schepanski et al. (2009b) suggest that dust source regions such as this are formed due to fluvial erosion process and high frequency of LLJs. The West African Heat Low controls the circulation in this area. During the simulation period, this emission area was active every day except for 27 and 29 May. Most of the high emission events occurred in the morning hours, when strong solar heating of the ground leads to convection and rapid growth of the Convective Boundary Layer (CBL) that allows downward momentum transport from the LLJs resulting in strong and gusty winds of 10–15 m s^{-1} (Knippertz et al., 2009a; Schepanski et al., 2009b).

Area *C* comprises the coastal areas of the western Sahara and spreads over the coastal belt from Boujdour (western Sahara) to Tantan (Morocco). Dust emissions in area *C* are simulated for 22–25 May. Most of the dust events occur between 1200 and 1800 UTC, which may be attributed to sea breeze in this coastal region. Tiris Zemmour has a high frequency of dust emission episodes and acts as the main source of fine-grained material in this region (Oberle, 2001; Varga, 2012).

Area *D* is located on the slopes of the Atlas Mountains. In this region, evaporative cooling associated with deep moist convection causes formation of DCs, while the High Atlas Mountain range serves as a trigger to the moist convection (Knippertz et al., 2007, 2009a). These systems frequently produce haboobs (Sutton, 1925; Membery, 1985; Knippertz et al., 2007). Knippertz et al. (2007) reported seven major DCs in the study region during the SAMUM-I campaign.

Area *E* is in the Senegal River basin where dust generates from overgrazing reactivated playas and ephemeral lakes (Gill, 1996; Ginoux et al., 2012).

Area *F* is in the upper Niger River basin where dust generated from alluvial sediments mostly results from overgrazing and sediments from seasonal flooding of the Niger River (Mulitza et al., 2010).

The model simulations suggest that most of the dust is emitted from areas A, B, and C during the simulation period. Areas E and F are remote with respect to the flight tracks and relatively unimportant for our analysis of the flight observations. The dust emissions in area D occur on 25–26 May and on 3 June.

In Fig. 6, the SD, bordered by a black dashed line, includes only source region D where most of the DCs take place. Therefore we also do calculations in the SD to quantify the contribution of DCs in the total optical depth in the SAMUM-I flight area.

3.2. *Spatial distribution of dust optical depth*

The radiative impact of the dust plume on energy balance and meteorology is characterised by AOD. At the same time AOD is the major observable characteristic that explains aerosol abundance and transport. At present only limited information about dust emission and deposition fluxes is available.

To demonstrate the model's capability to realistically simulate the dust plume, Fig. 7 compares the simulated and observed MODIS AOD. The spatial–temporal structure of the simulated and observed dust plumes compare well despite that the vast areas in the MODIS observations (shown in grey) are hidden by clouds. The aerosol plumes are quite extensive with optical depths exceeding 1. The high AOD on 25 and 26 May is attributed to emissions from areas A, B, F, and D (Fig. 7b and d). The model simulates strong dust emissions from area A from early morning to late evening. Dust in areas A and B is mobilised due to the presence of a subtropical cut-off centred low over northwest Africa accompanied by lee cyclone to the south of the Atlas Mountain range (not shown here), which causes strong northeasterly winds near the surface in the Chotts region. In area F, dust emissions occur during the mornings when the LLJ momentum mixes downwards, resulting in strong surface winds. DCs develop in late afternoons in region D. Despite that the model spatial resolution used in this study does not allow resolving single-cell moist convective updrafts explicitly, the model generates quite strong haboobs. This is in agreement with Reinfried et al. (2009), who showed that DCs develop well in regional simulations with Kain–Fritsch convective parameterisation (Kain and Fritsch, 1993) using 7 km grid spacing. Here we find that the Grell convective parameterisation (Grell and Dévényi, 2002) used in this study also allows DCs to develop at grid spacing of 5 km. The simulations in SD, which includes only D dust source region, show that haboobs in region D contribute about 30% of AOD at the AERONET station locations within SD (see Fig. 4a, b and c). The model presumably underestimates the intensity of DCs because deep convection is not explicitly resolved (Reinfried et al., 2009).

The MODIS AOD (Fig. 7a and b) is generally consistent with the model results. On 27 May there are no significant emissions from any of the dust source regions and most of the simulated AODs indicate remnants of the previous 2 d in the elevated dust layer (Fig. 7f). On 1 June the model simulates strong dust emission flux in the Chotts region (Area A) for the entire day caused by northeasterly winds. For a detailed description of the synoptic situation on these days, please see Knippertz (2008). The associated aerosol plume AOD on 1 June is shown in Fig. 7h. The main dust source regions on 3 June remain in areas B and F. On this day, emissions mostly occur between 0800 and 1100 UTC. Analysis of the wind field (not shown here) indicates that these emissions are caused by LLJ. The dust-laden air rapidly moves northward. This is reflected in the AOD for 3 June in both MODIS and WRF-Chem (Fig. 7i and j). In the Sahelian region (bottom of the domain at 15°N),

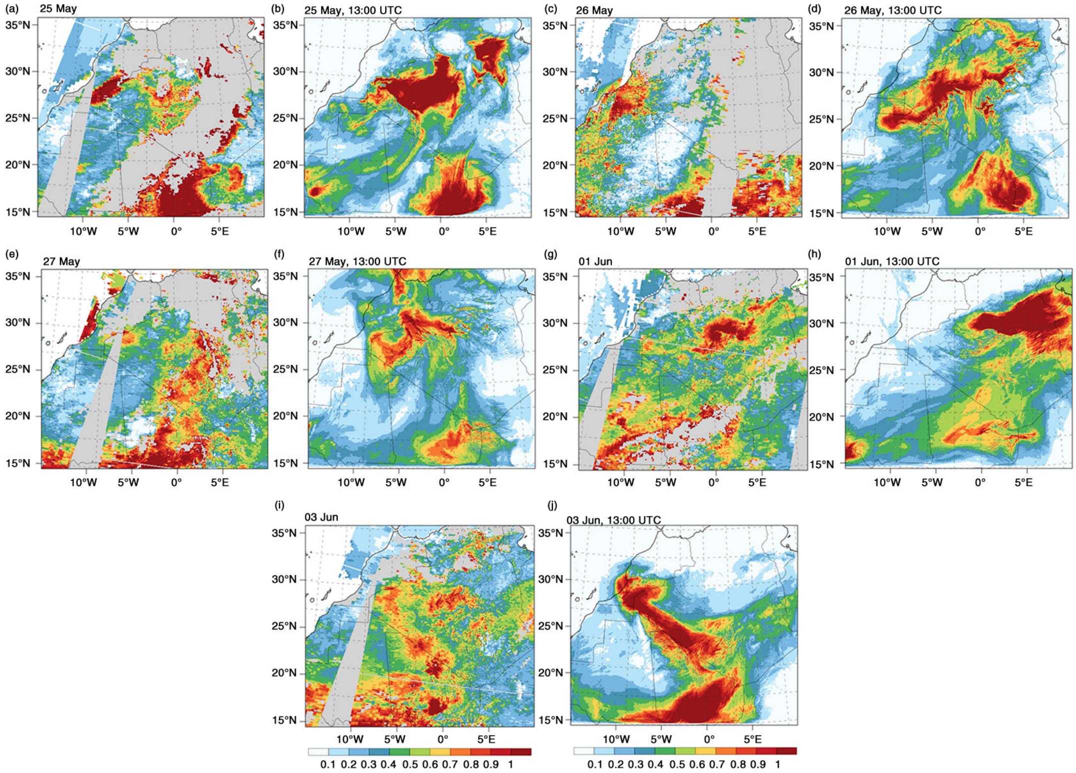

Fig. 7. Comparison of 0.55 µm AOD for the period of the SAMUM-I experiment from Terra-MODIS observations (a, c, e, g, i) and WRF-Chem (b, d, f, h, j) simulations at 0.6 µm. The MODIS plots for each date are generated by overlaying 3–5 images taken during a period from 10:00 to 13:00 UTC. The WRF-Chem AOD is shown at 13:00 UTC.

the model, consistent with MODIS, shows a well-developed plume from source regions E and F. The observed dust generation in region A, however, is missing in the simulations.

3.3. *Test of dust size distribution*

We evaluate aerosol size distributions in the framework of the SAMUM-I campaign, using model output and available airplane and ground-based observations.

3.3.1. *AERONET retrievals.* Figure 8 shows the AERONET Level 2.0 (red) at 07:07:41 UTC and simulated at 07:00 UTC (fine mode – green; coarse mode – black; and total – blue) column-integrated dust size distributions 2 hours prior to the research flight 060604a on 4 June 2006. The observed and simulated distributions are in good agreement. WRF-Chem underestimates the numbers of fine (0.1–0.2 µm) and coarse (3–10 µm) particles, and is fairly close to the observations in the range of particle diameters around 0.4–0.7 µm. These particles produce most of the radiative effect in visible range and therefore are well constrained by the 0.551 µm AOD that was tuned to be close to that observed by AERONET. The discrepancy for small particle diameters could be explained by the fact that AERONET retrievals tend to overestimate the number of small particles (McConnell et al., 2008). However, the discrepancy for large particles is probably because of the model's deficiency.

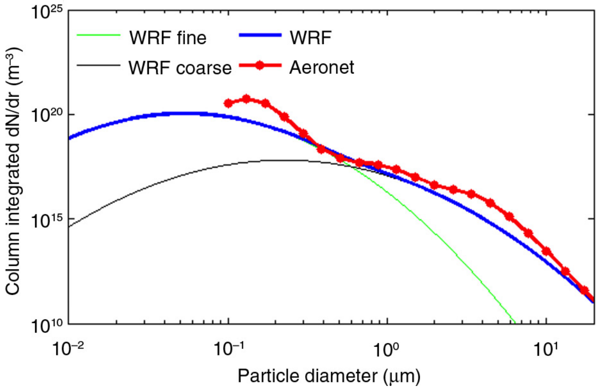

Fig. 8. Plot of column-integrated aerosol number size distributions (m^{-3}) from the WRF-Chem simulations at 7:00 UTC (green – fine mode; black – coarse mode; blue – total) and the AERONET Inversion Level 2.0 (red) at Ouarzazate at 7:07:41 UTC on 4 June 2006.

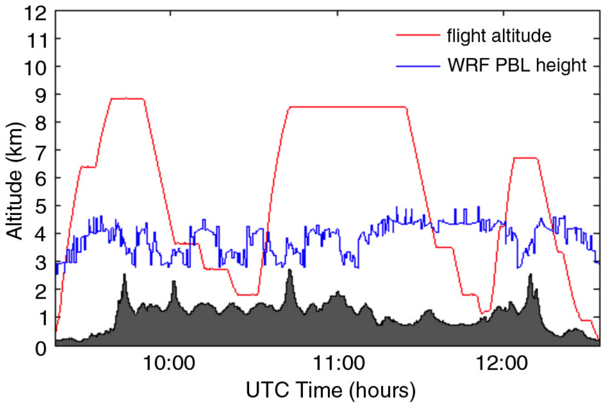

Fig. 9. Height (km) of the flight track as a function of time (solid magenta line) for SAMUM-I flight 060604a on 4 June 2006. Blue line shows the height of the PBL, which is calculated as a sum of CBL/NBL and RL. Grey shading shows the land elevation at the location of the aircraft.

3.3.2. SAMUM-I airplane observations. To further compare aerosol characteristics along the DLR Falcon flight tracks, we analysed 12 flights during the simulation period. While all of them capture similar general behaviours and compare well with WRF-Chem simulations, flight 060604a was chosen for demonstration due to its extended duration and the richest distribution of sampled altitudes. The complete description of the flights is given in Weinzierl et al. (2009).

Flight 060604a took off on 4 June at 09:18 UTC from Casablanca airport located near the Atlantic coast, crossed over the Atlas Mountains, continued to the Ouarzazate site, then moved to Zagora, and returned back to Casablanca at 12:34 UTC. Figure 9 shows the flight altitudes as a function of time, the land elevation at the location of the airplane, as well as the height of the Planetary Boundary Layer.

Instrumental observations of aerosol size distributions on the airplane during the SAMUM-I campaign were conducted by a set of instruments including a Forward Scattering Spectrometer Probe (FSSP-300, FSSP-100), a Passive Cavity Spectrometer Probe (PCASP), a set of condensation particle counters (CPC/CPSA) operated at different lower cut-off diameters, a Grimm Optical Particle Counter (Grimm OPC), and a Differential Mobility Analyzer (DMA) (Weinzierl et al., 2009). For use in models, Weinzierl et al. (2009) also approximated the observed

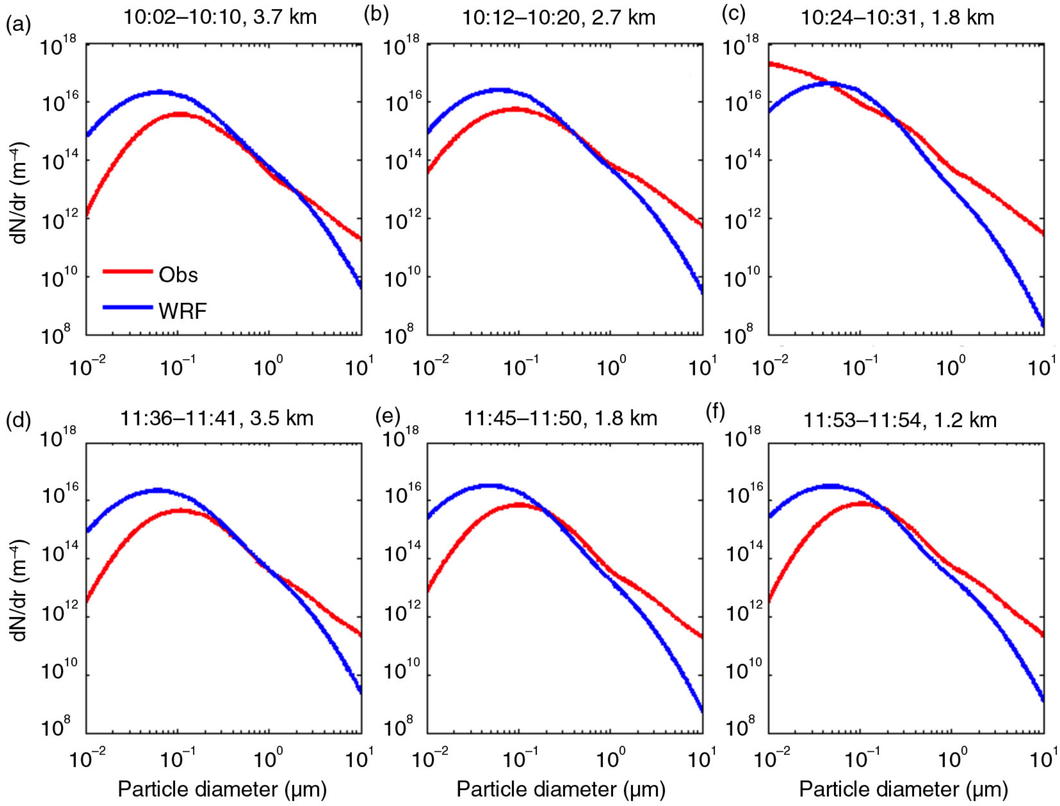

Fig. 10. Plots of the simulated (blue) and observed (red) aerosol number–size distribution (m^{-4}) averaged in time over the constant height elements of the airplane track during research flight 060604a on 4 June 2006. The observed time intervals and the heights of the elements of the flight track are shown in the titles of each panel. The simulated size distributions are sampled at corresponding locations at 10:00 UTC (a–c) and at 11:00 UTC (d–f) on 4 June 2006.

aerosol size distributions by four log-normal modes and reported their parameters. These distributions are listed in Table 4 of Weinzierl et al. (2009). We use that information to compare the simulated and observed aerosol size distributions along those time intervals of the flight track in Fig. 9, where the height is constant (see Fig. 10). All chosen heights are within the PBL. For all six time intervals in Fig. 10, the simulated and observed size distributions

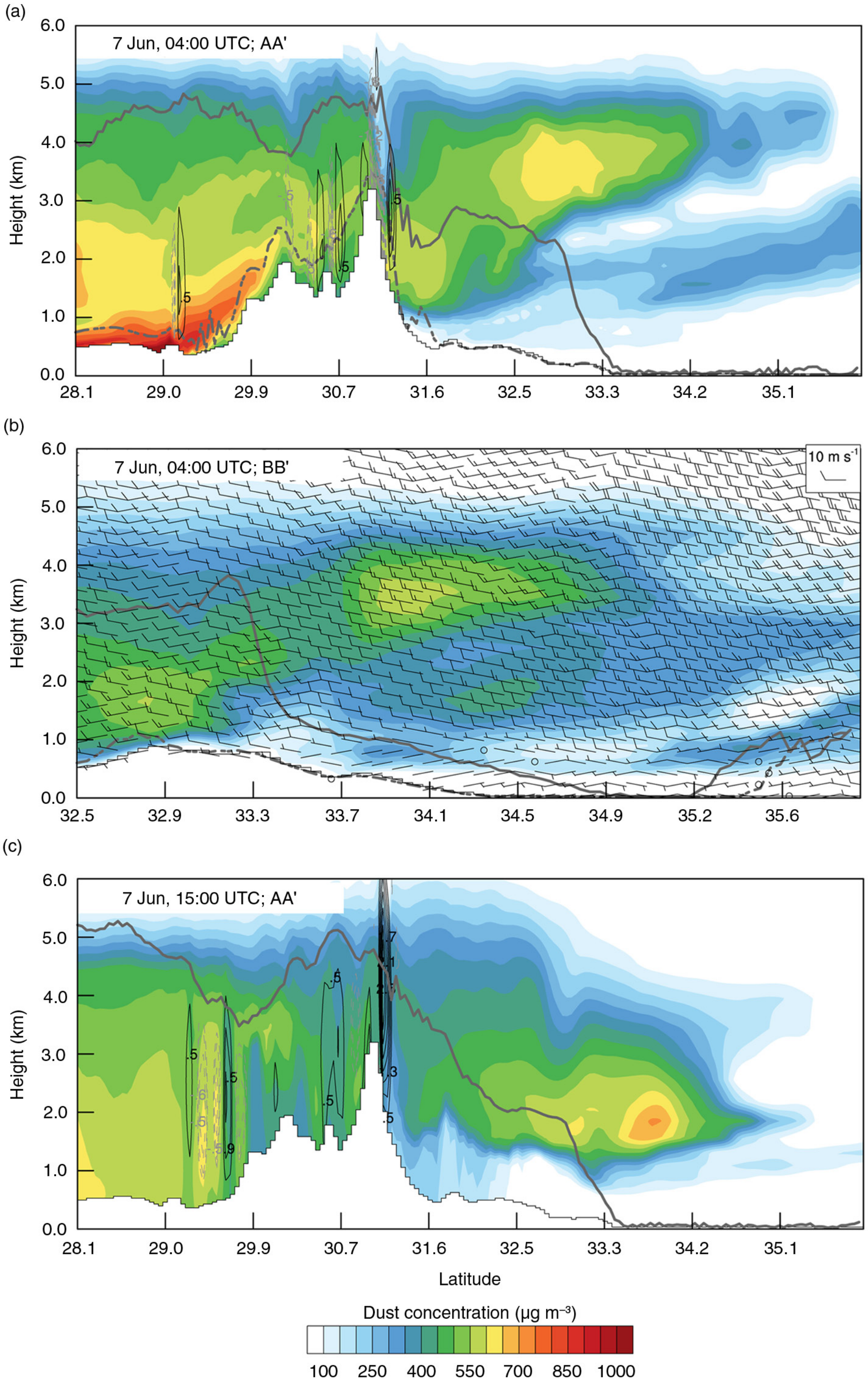

Fig. 11. (*Continued*)

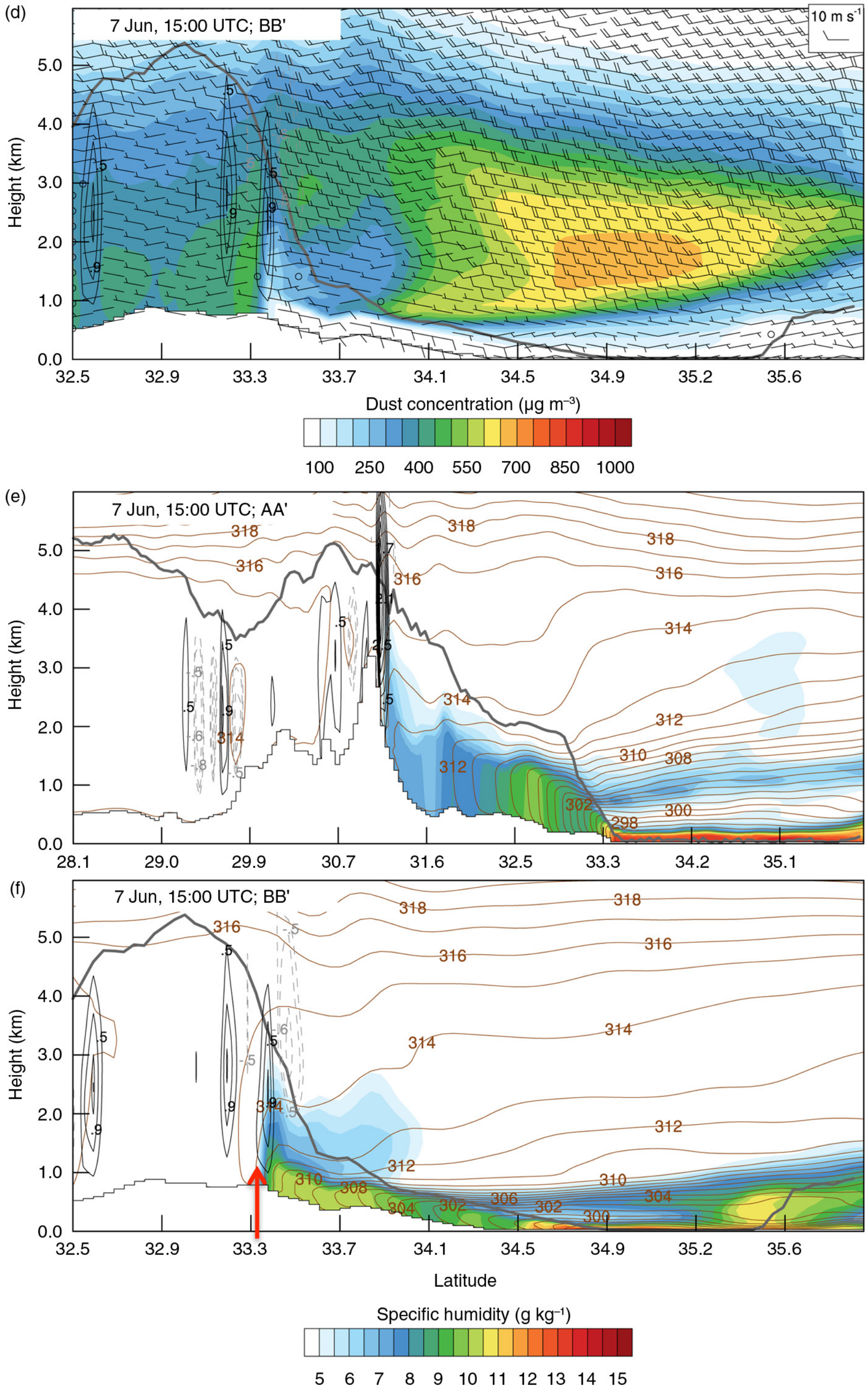

Fig. 11. (a) Dust concentration (shaded, µg m^{-3}), height of the nocturnal boundary layer (dashed grey line, km), vertical velocity (m s^{-1}; upward – black solid line; and downward – grey dashed line) at the AA′ meridional cross-section on 7 June 2006 at 04:00 UTC; the solid grey line shows the height of the PBL (km) at 15:00 UTC the day before 6 June that we associate with the RL height in the morning; (b) same as (a) but for BB′ cross-section and (V,W) wind barbs (m s^{-1}); (c) same as (a) but on 7 June 2006 at 15:00 UTC and the PBL height is shown for 7 June 2006 at 15:00 UTC; (d) same as (b) but on 7 June 2006 at 15:00 UTC and the PBL height is shown for 7 June 2006 at 15:00 UTC; (e) specific humidity (g kg^{-1}) and potential temperature (K, contour lines) in the AA′ cross-section on 7 June 2006; (f) same as (e) but for the BB′ cross-section.

compare well for most optically active (for visible wave lengths) aerosol diameters, 0.3–0.7 μm. However, the model overestimates the number of very fine particles (contrary to what was observed in comparison with AERONET (see Fig. 8) and underestimates the number of large particles (similar to what was observed in comparison with AERONET in Fig. 8). It is worth mentioning that MADE/SORGAM is a modal aerosol model and, by design, is unable to account for the giant particles of 30–50 μm diameter observed by Weinzierl et al. (2009), as it assumes that particles to follow a two-mode log-normal size distribution (2) with the fixed width (3).

Laurent et al. (2010) and Heinold et al. (2009) calculated aerosol size distributions during the SAMUM-I campaign using a five-bin microphysical model. They obtain a good agreement with AERONET and Falcon observations for particle sizes of 1–20 μm but underestimate the number of very fine particles with diameters of 0.1–0.2 μm. They argue that small particles might have a non-dust origin. In our simulations, we see that the fine aerosol mode weakens when the mass emission of small dust particles decreases. However, in both simulations the contribution of coarse dust mode in the AOD is dominant.

3.4. *Dust plume formation over the ocean*

Long-range cross-Atlantic transport of Saharan dust in the Saharan Air Layer (SAL), located above the marine boundary layer, is well documented (Prospero et al., 2002; Chen et al., 2010; Drame et al., 2011). Here, advantage is taken of SAMUM-I observations to understand the formation of an aerosol plume over the Atlantic Ocean in the study region at the Moroccan coast. A 5 km deep dust layer is simulated on 3–4 June both to the south and the north of the Atlas Mountains. However, northward dust transport occurs only on 6–7 June.

During the mid-morning on 5 and 6 June, the model simulates two medium level dust outbreaks. The first dust outbreak on 5 June is initiated by emissions from the hydro-dust source area A (Fig. 6), under strong easterly/northeasterly winds. The second dust outbreak on 6 June is driven by emissions from source area B (Fig. 6) to the west of the Ahaggar Mountains at 25.5°N, 3.0°E under strong northeasterly winds. On 6–7 June the uplifted dust is transported to the north of the High Atlas Mountains by southerly/southwesterly winds.

To better demonstrate the formation of the aerosol plume, Fig. 11 shows meteorological characteristics and the dust concentration in two latitude–height cross-sections at longitudes of 7.79°W (AA′ cross-section, Fig. 11a, c and e) and 6.3°W (BB′ cross-section, Fig. 11b, d and f) on 7 June at 4:00 UTC, when the land breeze is not ceased yet, and at 15:00 UTC, when the sea breeze fully develops. The AA′ cross-section goes through the Atlas Mountains with elevation above 3 km. The BB′ cross-section covers the area closer to the ocean behind the mountains where the elevation does not exceed 1 km.

The solid lines in Fig. 11a–f depict the height of the Residual Layer (RL) calculated as the maximum height of the Planetary Boundary Layer in the previous diurnal cycle. The dashed lines in Fig. 11a and b show the depth of the shallow nocturnal boundary layer (NBL). The vertical velocity contours in Fig. 11a–f show the regions of vertical motion (vertical velocity is shown by solid black (updrafts) and dashed grey (downdrafts) contours) that could mix dust above PBL. The wind barbs in Fig. 11b show the predominant southerly flow in the lower troposphere and the land breeze near the surface. The CBL, which by 15:00 UTC has consumed the RL, reaches the height of PBL.

In the morning (Fig. 11a and b) before crossing the High Atlas Mountains, most dust is confined to the 4 km high RL over land. The orographic lifting on the southern side of the Atlas Mountains, as well as the convection developed on the slopes cause some of the dust-laden air to escape the RL (Fig. 11a and b). The orographic lifting effect of the Atlas Mountains was well observed by the airborne lidar observations discussed in Esselborn et al. (2009) and Heinold et al. (2009).

At night or in early morning, most dust is transported northward in the RL by prevailing large-scale southerly winds and land breezes towards the ocean. In the region of the strong gradient of the RL height in the coastal area and the weak night inversion between RL and the free troposphere, it mixes up into the free troposphere relatively easily.

The growth of the CBL in the morning entrains aerosols in the RL over the land but does not affect the aerosol plume over the ocean, as the marine PBL is very shallow. In the afternoon, the fully developed PBL at 15:00 UTC is much higher over land (about 5 km) than over sea (200–300 m) with a steep gradient of PBL height and all meteorological characteristics in a transition coastal zone between land and sea (Fig. 11d–f). A strong convection develops over the Atlas Mountains (Fig. 11c). This convection mixes the dust-laden layer from the PBL into the free troposphere, eroding the capping inversion. The sea breeze strengthens by 15:00 UTC (Fig. 11e and f). Its propagation is well marked by transport of moisture and potential temperature. The breeze front reaches 31°N in Fig. 11e and 33.3°N in Fig. 11f. The updrafts in the breeze front also cause mixing dust across the PBL top in the free troposphere.

3.5. *Interaction of sea breezes with continental dust outflow*

The SAMUM-I observations show the formation of the elevated aerosol layer over the sea that is clearly detached from the surface. We were able to reproduce this effect in our simulations and found that the interaction of the coastal outflow with the breeze plays an important role. Sea breezes are known for trapping pollutants emitted from the surface layer of the coastal regions (e.g. McKendry, 1989; Miller et al., 2003). WRF-Chem simulates sea breezes from 10:00 to 19:00 UTC at the Moroccan coast of the Atlantic Ocean. Figure 11e and f show the vertical cross-sections of land and sea at 15:00 UTC. The potential temperature indicates the sea-breeze inflow layer depth and its horizontal extent, while the water vapour mixing ratio shows the difference in moisture content between the cold dense marine air and the warm dry land air. The average height of the landward branch of the simulated sea breeze ranges from 0.7 to 1 km above ground level (agl), while the wind speed within the sea-breeze flow varies from 8 to 13 m s^{-1}. The inland extent of the sea breeze reaches 100–150 km (Fig. 11e and f). The water vapour mixing ratio in the sea-breeze flow ranges from 15 g kg^{-1} in the first 150 m over the sea to 7.5 g kg^{-1} over land. Strong updrafts up to 1.5 m s^{-1} form due to convergence between the sea-breeze air and land air along the frontal zone. Perturbations in the sea-breeze front grow in height from 2.0 to 3.5 km, nearing the top of the PBL in the coastal area (Fig. 11c–f). Behind the sea-breeze front, the warm air over-rides the marine air and forms a strong inversion above the cold and moist landward flow. Due to this inversion, the relatively warm dusty air is unable to mix downward. The air that is uplifted in the sea-breeze convergence zone rapidly moves above the breeze flow seawards with strong northward prevailing winds. The landward branch of the breeze effectively cleans the lower part of the dust plume over the sea, detaching the aerosol layer from the sea surface as observed (see Fig. 11d).

To further demonstrate this point Fig. 12 presents the vertical profiles of wind and dust concentrations at 6.3°W, 33.5°N (this position is indicated in Fig. 11f). This location is approximately 150 km inland from the coastline with a land elevation of 500 m. Figure 12a shows rotation of the surface winds across the diurnal cycle. The day time heating forms a well-mixed deep PBL at around 13:00 UTC with a westerly flow near the surface and a southerly flow above 2.0 km. At 15:00 UTC, the simulated sea-breeze front arrived at this location. The cold marine air forms a shallow internal boundary layer while the wind rotates and comes at a right angle (northwest) to the coastline. Wind maxima reach 7–9 m s^{-1} at 1000 m, and wind minima around 1500 m asl (Fig. 12b) marks the top of the internal boundary layer that is attributed to sea-breeze inflow layer.

A distinct feature of the dust profiles in Fig. 12c (from 4:00 to 15:00 UTC) is the gradual decrease of the dust concentration in the surface layer. Before the arrival of the sea breeze, at 4:00 UTC the dust concentration reaches 400 μg m^{-3} in the surface layer below 1500 m. It decreases at 13:00 and 15:00 UTC till 200 and 100 μg m^{-3}, respectively, while changing little in the 1500–2500 m layer.

3.6. *Dust partitioning between the PBL and the free troposphere*

Over land, dust particles are first entrained into the surface layer and then during the day they mix in the CBL that, at about 15:00–16:00 UTC, reaches its maximum height and consumes the RL. At night, the PBL collapses, a shallow NBL develops instead, but most of airborne dust remains in the RL. However, in the morning hours, the growing CBL rapidly erodes the RL and entrains the previous day's uplifted dust. Therefore, at any given time most of the dust mass stays in the PBL, where the PBL consists of NBL or CBL and RL. The height of the PBL over land is 4–5 km in the present simulations. This is in a good agreement with the SAMUM-I airborne lidar observations aboard the Falcon airplane (Esselborn et al., 2009; Heinold et al., 2009; Laurent et al., 2010).

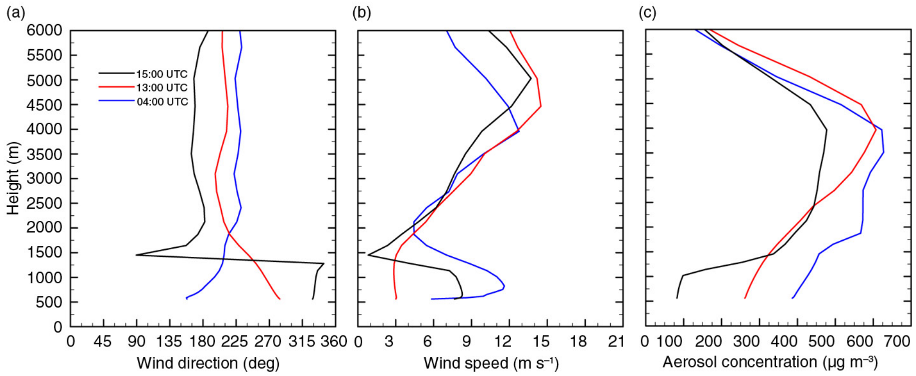

Fig. 12. Vertical profiles of (a) wind direction (degrees), (b) wind speed (m s^{-1}), (c) aerosol concentration (μg m^{-3}) on 7 June 2006 at 04:00, 13:00 and 15:00 UTC in the location of 6.3°W, 33.35°N as indicated by the red arrow in Fig. 11f.

Because of turbulent mixing, the lifetime of dust particles in the PBL is relatively short, while particles above the top of the PBL are disconnected from the surface and could stay in the free troposphere for extended times, which would be sufficient for long-range transport. To better quantify partitioning of the dust mass between the PBL and the free troposphere, we calculated the average dust loadings in and above the top of the PBL (that includes RL) separately over land and over sea areas in the LD (Fig. 13). The maximum loading over land is about 1.2 g m^{-2}, and over the ocean is 0.5 g m^{-2}. Over land, about 10–15% of the dust is in the free troposphere. Over the ocean, the dust loading in the free troposphere greatly exceeds that in the shallow marine boundary layer. This is in good agreement with the analysis conducted in the previous section.

4. Summary and conclusions

In this study, we use the WRF-Chem model along with observational data from SAMUM-I to investigate dust generation, vertical mixing, and transport from the north-west Sahara towards the North Atlantic Ocean and Mediterranean Sea. We use finer grid spacing than in previous studies (Heinold et al., 2009; Laurent et al., 2010), which makes the simulations computationally demanding. Therefore, we employ a relatively simple and fast modal microphysical model, MADE/SORGAM, and test it for the SAMUM-I conditions.

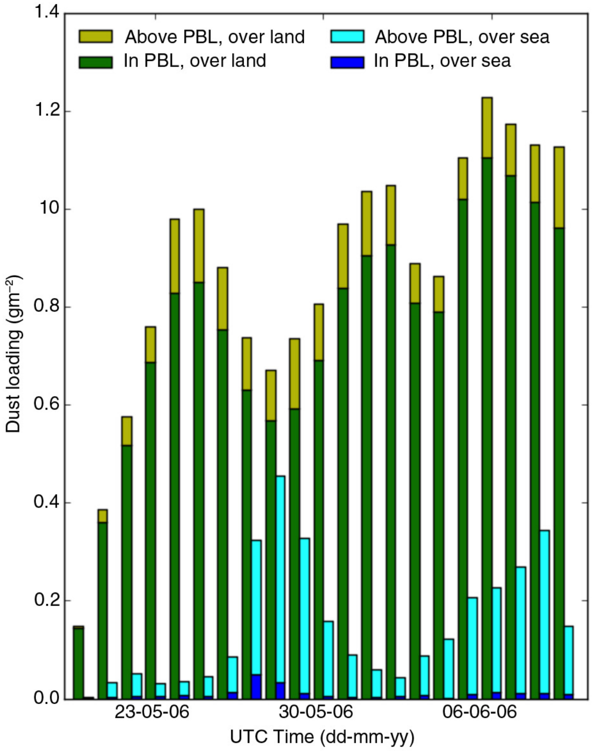

Fig. 13. Bar chart of the domain average daily mean dust loadings (g m^{-2}) in the free troposphere and in the PBL over land (dark and light green) and over the ocean (dark and light blue) as functions of time.

WRF-Chem simulates well the meteorological fields and major dust outbreaks observed during the simulation period. Dust source areas are activated in agreement with the previous studies. The chosen domain includes all major dust source areas activated during the study period. The observed single scattering albedo and Angstrom exponent suggest that dust prevails the aerosol radiation effect. In the SAMUM-I observation area, the contribution of non-dust aerosols to total optical depth does not exceed 2–3%. The sea salt effect is seen over sea and along the narrow coastal area, but sea salt load, even over the sea, is 100 times smaller than that for dust.

The orographic lifting of dust over the Atlas Mountains, convection on the mountain slopes and updrafts in the breeze front, as well as transport of dust from the PBL into the free troposphere in the land/sea transition zone are the most effective mechanisms of dust penetration into the free troposphere. Interaction of continental outflow with sea breeze is a key process that leads to formation of a surface-detached dust plume over the marine boundary layer. This mechanism should be applicable to formation of SAL. Over land WRF-Chem predicts 10–15% dust load in the free troposphere, 85–90% in PBL, but over the Atlantic Ocean the free troposphere fraction of dust load could be more than 90%.

The model produces realistic spatial–temporal distributions of AOD compared with the MODIS satellite and AERONET ground observations. Despite that the model grid spacing used is not sufficient to explicitly resolve deep convection, the model equipped with the Grell convective parameterisation simulates haboobs in the right region and at right time. However, it might underestimate their intensity. Simulations conducted in a smaller domain that include only haboob dust sources suggest that haboobs were responsible for 1/3 of dust generation in the SAMUM-I observation region.

The model dust emission scheme is tuned to simultaneously fit the observed total optical depth and the ratio of AODs generated by fine and coarse dust modes. WRF-Chem, both in comparison with AERONET retrievals and SAMUM-I instrumental observations, predicts well the number density of the most optically active particles with diameters of 0.4–0.7 μm. However, its modal microphysical model is unable to correctly reproduce the tails of the dust size distribution, overestimating the number density of small particles and underestimating the number density of large particles. More sophisticated multimode or bin aerosol microphysical models should be employed to resolve these tail effects.

5. Acknowledgements

The authors would like to thank the Principal Investigators (P.I.s) of the four AERONET sites for making available the AERONET data used in this study: Emilio Cuevas-Agullo and M. Taoufik Zaidouni, P.I.s for Ouarzazate; Bernard Mougenot and Olivier Hagolle, P.I.s for Ras-El-Ain; Bernard Mougenot and Benoit Duchemin, P.I.s for Saada; Emilio Cuevas-Agullo and Juan Cuesta, P.I.s for Tamanrasset. The research reported in this publication was supported by King Abdullah University of Science and Technology (KAUST). For computer time, this research used the resources of the KAUST Supercomputing Laboratory. B.W. thanks funding by the Helmholtz Association under grant number VH-NG-606 (Helmholtz-Hochschul-Nachwuchsforschergruppe AerCARE).

References

Ackermann, I. J., Hass, H., Memmesheimer, M., Ebel, A., Binkowski, F. S. and co-authors. 1998. Modal aerosol dynamics model for Europe: development and first applications. *Atmos. Environ*. **32**, 2981–2999.

Ashpole, I. and Washington, R. 2013a. Intraseasonal variability and atmospheric controls on daily dust occurrence frequency over the central and western Sahara during the boreal summer. *J. Geophys. Res. Atmos*. **118**, 12915–12926.

Ashpole, I. and Washington, R. 2013b. A new high-resolution central and western Saharan summertime dust source map from automated satellite dust plume tracking. *J. Geophys. Res. Atmos*. **118**, 6981–6995.

Chen, S.-H., Wang, S.-H. and Waylonis, M. 2010. Modification of Saharan air layer and environmental shear over the eastern Atlantic Ocean by dust-radiation effects. *J. Geophys. Res. Atmos*. **115**, D21202.

Chin, M., Ginoux, P., Kinne, S., Torres, O., Holben, B. N. and co-authors. 2002. Tropospheric aerosol optical thickness from the GOCART model and comparisons with satellite and sun photometer measurements. *J. Atmos. Sci*. **59**, 461–483.

Cuesta, J., Marsham, J. H., Parker, D. J. and Flamant, C. 2009. Dynamical mechanisms controlling the vertical redistribution of dust and the thermodynamic structure of the West Saharan atmospheric boundary layer during summer. *Atmos. Sci. Lett*. **10**, 32–42.

Dee, D. P., Uppala, S. M., Simmons, A. J., Berrisford, P., Poli, P. and co-authors. 2011. The ERA-Interim reanalysis: configuration and performance of the data assimilation system. *Q. J. Roy. Meteorol. Soc*. **137**, 553–597.

Dinter, T., Hoyningen-Huene, W. V., Burrows, J., Kokhanovsky, A., Bierwirth, E. and co-authors. 2009. Retrieval of aerosol optical thickness for desert conditions using MERIS observations during the SAMUM campaign. *Tellus B*. **61**, 229–238.

Donnell, E., Fish, D. J., Dicks, E. M. and Thorpe, A. J. 2001. Mechanisms for pollutant transport between the boundary layer and the free troposphere. *J. Geophys. Res*. **106**, 7847–7856.

Drame, M., Jenkins, G. S., Camara, M. and Robjhon, M. 2011. Observations and simulation of a Saharan air layer event with a midtropospheric dust layer at Dakar, Senegal, 6–7 July 2010. *J. Geophys. Res. Atmos*. **116**, D21204.

Dubovik, O., Sinyuk, A., Lapyonok, T., Holben, B. N., Mishchenko, M. and co-authors. 2006. Application of spheroid models to account for aerosol particle nonsphericity in remote sensing of desert dust. *J. Geophys. Res. Atmos*. **111**, D11208.

Eck, T. F., Holben, B. N., Reid, J. S., Dubovik, O., Smirnov, A. and co-authors. 1999. Wavelength dependence of the optical depth of biomass burning, urban, and desert dust aerosols. *J. Geophys. Res*. **104**, 31333–31349.

Emmel, C., Knippertz, P. and Schulz, O. 2010. Climatology of convective density currents in the southern foothills of the Atlas Mountains. *J. Geophys. Res*. **115**, 11.

Engelstaedter, S. and Washington, R. 2007. Atmospheric controls on the annual cycle of North African dust. *J. Geophys. Res. Atmos*. **112**, D03103.

Esselborn, M., Wirth, M., Fix, A., Weinzierl, B., Rasp, K. and co-authors. 2009. Spatial distribution and optical properties of Saharan dust observed by airborne high spectral resolution lidar during SAMUM 2006. *Tellus B*. **61**, 131–143.

Fiedler, S., Schepanski, K., Knippertz, P., Heinold, B. and Tegen, I. 2014. How important are atmospheric depressions and mobile cyclones for emitting mineral dust aerosol in North Africa? *Atmos. Chem. Phys*. **14**, 8983–9000.

Flamant, C., Chaboureau, J.-P., Parker, D. J., Taylor, C. M., Camma, J.-P. and co-authors. 2007. Airborne observations of the impact of a convective system on the planetary boundary layer thermodynamics and aerosol distribution in the inter-tropical discontinuity region of the West African Monsoon. *Q. J. R. Meteorol. Soc*. **133**, 1175–1189.

Freitas, S. R., Longo, K. M., Alonso, M. F., Pirre, M., Marecal, V. and co-authors. 2011. PREP-CHEM-SRC – 1.0: a preprocessor of trace gas and aerosol emission fields for regional and global atmospheric chemistry models. *Geosci. Model Dev*. **4**, 419–433.

Gamo, M. 1996. Thickness of the dry convection and large-scale subsidence above deserts. *Bound. Layer Meteorol*. **79**, 265–278.

Gill, T. E. 1996. Eolian sediments generated by anthropogenic disturbance of playas: human impacts on the geomorphic system and geomorphic impacts on the human system. *Geomorphology*. **17**, 207–228.

Ginoux, P., Chin, M., Tegen, I., Prospero, J. M., Holben, B. and co-authors. 2001. Sources and distributions of dust aerosols simulated with the GOCART model. *J. Geophys. Res*. **106**, 19.

Ginoux, P., Prospero, J. M., Gill, T. E., Hsu, N. C. and Zhao, M. 2012. Global-scale attribution of anthropogenic and natural dust sources and their emission rates based on MODIS deep blue aerosol products. *Rev. Geophys*. **50**, 1–36, Paper number 2012RG000388.

Grell, G. and Dévényi, D. 2002. A generalized approach to parameterizing convection combining ensemble and data assimilation techniques. *Geophys. Res. Lett*. **29**, 38-31–38-34.

Grell, G., Peckham, S. E., Schmitz, R., McKeen, S. A., Frost, G. and co-authors. 2005a. Fully coupled ''online'' chemistry within the WRF model. *Atmos. Environ.* **39**, 6957–6975.

Grell, G. A., Peckham, S. E., Schmitz, R., McKeen, S. A. and Frost, G. J. 2005b. The WRF-chemistry air quality model: updates, improvements and evaluation. In: *Proceedings of the 6th WRF/15th MM5 Users' Workshop*, San Diego, pp. 1–31.

Heinold, B., Knippertz, P., Marsham, J. H., Fiedler, S., Dixon, N. S. and co-authors. 2013. The role of deep convection and nocturnal low-level jets for dust emission in summer time West Africa: estimates from convection-permitting simulations. *J. Geophys. Res. Atmos.* **118**, 4385–4400.

Heinold, B., Tegen, I. N. A., Esselborn, M., Kandler, K., Knippertz, P. and co-authors. 2009. Regional Saharan dust modelling during the SAMUM 2006 campaign. *Tellus B.* **61**, 307–324.

Heintzenberg, J. 2008. The SAMUM-1 experiment over Southern Morocco: overview and introduction. *Tellus B.* **61**, 2–11.

Holben, B. N., Eck, T. F., Slutsker, I., Tanre, D., Buis, J. P. and co-authors. 1998. AERONET – a federated instrument network and data archive for aerosol characterization. *Rem. Sens. Environ.* **66**, 1–16.

Holben, B. N., Tanre, D., Smirnov, A., Eck, A. and Slutsker, I. 2001. An emerging groundbased aerosol climatology: aerosol optical depth from AERONET. *J. Geophys. Res.* **106**, 12067–12097.

Hsu, N. C., Tsay, S. C., King, M. D. and Herman, J. R. 2004. Aerosol properties over bright-reflecting source regions. *IEEE Trans. Geosci. Rem. Sens.* **42**, 557–569.

Kain, J. and Fritsch, J. M. 1993. Convective parameterization for mesoscale models: the Kain–Fritsch scheme. In: *The Representation of Cumulus Convection in Numerical Models* (eds. K. Emanuel and D. Raymond). American Meteorological Society, Boston, Massachusetts, pp. 165–170.

Kalenderski, S., Stenchikov, G. and Zhao, C. 2013. Modeling a typical winter-time dust event over the Arabian Peninsula and the Red Sea. *Atmos. Chem. Phys.* **13**, 1999–2014.

Kalu, A. E. 1979. The African dust plume: its characteristics and propagation across West Africa in Winter. In: *Saharan Dust* (ed. C. Morales). Wiley, Chichester, pp. 95–118.

Kandler, K., Schutz, L., Deutscher, C., Ebert, M., Hofmann, H. and co-authors. 2009. Size distribution, mass concentration, chemical and mineralogical composition and derived optical parameters of the boundary layer aerosol at Tinfou, Morocco, during SAMUM 2006. *Tellus B.* **61**, 32–50.

Knippertz, P. 2008. Dust emissions in the West African heat trough – the role of the diurnal cycle and of extratropical disturbances. *Meteorol. Z.* **17**, 553–563.

Knippertz, P., Ansmann, A., Althausen, D., Muller, D., Tesche, M. and co-authors. 2009a. Dust mobilization and transport in the northern Sahara during SAMUM 2006 – a meteorological review. *Tellus B.* **61**, 12–31.

Knippertz, P., Deutscher, D., Kandler, K., Muller, T., Schulz, O. and co-authors. 2007. Dust mobilization due to density currents in the Atlas region: observations from the Saharan mineral dust experiment 2006 field campaign. *J. Geophys. Res.* **112**, D21109.

Knippertz, P. and Fink, A. H. 2006. Synoptic and dynamic aspects of an extreme springtime Saharan dust outbreak. *Q. J. Roy. Meteorol. Soc.* **132**, 1153–1177.

Knippertz, P. and Stuut, J. B. 2014. *Mineral Dust, A key player in the Earth System*. Springer, New York.

Knippertz, P., Trentmann, J. and Seifert, A. 2009b. High-resolution simulations of convective cold pools over the northwestern Sahara. *J. Geophys. Res. Atmos.* **114**, D08110.

Koch, J. and Renno, N. O. 2005. The role of convective plumes and vortices on the global aerosol budget. *Geophys. Res. Lett.* **32**, 1–5.

Kok, J. F. 2011a. A scaling theory for the size distribution of emitted dust aerosols suggests climate models underestimate the size of the global dust cycle. *Proc. Natl. Acad. Sci. U. S. A.* **108**, 1016–1021.

Kok, J. F. 2011b. Does the size distribution of mineral dust aerosols depend on the wind speed at emission? *Atmos. Chem. Phys.* **11**, 10149–10156.

Kok, J. F., Parteli, E. J. R., Michaels, T. I. and Karam, D. B. 2012. The physics of wind-blown sand and dust. *Rep. Prog. Phys.* **75**, 106901.

Laurent, B., Tegen, I., Heinold, B., Schepanski, K., Weinzierl, B. and co-authors. 2010. A model study of Saharan dust emissions and distributions during the SAMUM-1 campaign. *J. Geophys. Res.* **115**, D21210.

Mahowald, M. N., Bryant, R. G., Corral, D. J. and Steinberger, L. 2003. Ephemeral lakes and desert dust sources. *Geophys. Res. Lett.* **30**, 2(1074).

Marsham, J. H., Parker, D. J., Grams, C. M., Johnson, B. T., Grey, W. M. F. and co-authors. 2008. Observations of mesoscale and boundary-layer scale circulations affecting dust transport and uplift over the Sahara. *Atmos. Chem. Phys.* **8**, 6979–6993.

Marticorena, B. and Bergametti, G. 1995. Modeling the atmospheric dust cycle: 1. Design of a soil-derived dust emission scheme. *J. Geophys. Res. Atmos.* **100**, 16415–16430.

McConnell, C. L., Highwood, E. J., Coe, H., Formenti, P., Anderson, B. and co-authors. 2008. Seasonal variations of the physical and optical characteristics of Saharan dust: results from the Dust Outflow and Deposition to the Ocean (DODO) experiment. *J. Geophys. Res.* **113**, D14S05.

McKeen, S. A., Wotawa, G., Parrish, D. D., Holloway, J. S., Buhr, M. P. and co-authors. 2002. Ozone production from Canadian wildfires during June and July of 1995. *J. Geophys. Res.* **107**, 4192.

McKendry, I. G. 1989. Numerical simulation of sea breezes over the Auckland region, New Zealand – air quality implications. *Bound. Layer Meteorol.* **49**, 7–22.

Membery, D. A. 1985. A gravity wave haboob. *Weather.* **40**, 214–221.

Miller, S. T. K., Keim, B. D., Talbot, R. W. and Mao, H. 2003. Sea breeze: structure, forecasting, and impacts. *J. Geophys. Res.* **41**, 31.

Mulitza, S., Heslop, D., Pittauerova, D., Fischer, H. W., Meyer, I. and co-authors. 2010. Increase in African dust flux at the onset of commercial agriculture in the Sahel region. *Nature.* **466**, 226–228.

Müller, D., Lee, K. H., Gasteiger, J., Tesche, M., Weinzierl, B. and co-authors. 2012. Comparison of optical and microphysical properties of pure Saharan mineral dust observed with AERONET sun photometer, Raman lidar, and in situ instruments during SAMUM 2006. *J. Geophys. Res. Atmos.* **117**, D07211.

Oberle, F. 2001. *Monitoring of Easterly Saharan Dust Storms*. University of Hawaii, Manoa.

Otto, S., Reus, M. D., Trautmann, T., Thomas, A., Wendisch, M. and co-authors. 2007. Atmospheric radiative effects of an in situ measured Saharan dust plume and the role of large particles. *Atmos. Chem. Phys.* **7**, 4887–4903.

Petzold, A., Rasp, K., Weinzierl, B., Esselborn, M., Hamburger, T. and co-authors. 2009. Saharan dust absorption and refractive index from aircraft-based observations during SAMUM 2006. *Tellus B*. **61**, 118–130.

Prakash, P. J., Stenchikov, G., Kalenderski, S., Osipov, S. and Bangalath, H. 2015. The impact of dust storms on the Arabian Peninsula and the Red Sea. *Atmos. Chem. Phys.* **15**, 199–222.

Prospero, J. M., Ginoux, P., Torres, O., Nicholson, S. E. and Gill, T. E. 2002. Environmental characterization of global sources of atmospheric soil dust identified with the NIMBUS 7 total ozone mapping spectrometer (TOMS) absorbing aerosol product. *Rev. Geophys.* **40**, 31.

Randerson, J. T., van der Werf, G. R., Giglio, L., Collatz, G. J. and Kasibhatla, P. S. 2007. *Global Fire Emissions Database, Version 2 (GFEDv2.1)*. Oak Ridge National Laboratory Distributed Active Archive Center, Oak Ridge, TN.

Reinfried, F., Tegen, I., Heinold, B., Hellmuth, O., Schepanski, K. and co-authors. 2009. Simulations of convectively-driven density currents in the Atlas region using a regional model: impacts on dust emission and sensitivity to horizontal resolution and convection schemes. *J. Geophys. Res. Atmos.* **114**, D08127.

Remer, L. A., Kaufman, Y. J., Tanré, D., Mattoo, S., Chu, D. A. and co-authors. 2005. The MODIS aerosol algorithm, products and validation. *J. Atmos. Sci.* **62**, 947–973.

Remer, L. A., Kleidman, R. G., Levy, R. C., Kaufman, Y. J., Tanré, D. and co-authors. 2008. Global aerosol climatology from the MODIS satellite sensors. *J. Geophys. Res.* **113**, D14S07.

Ryder, C. L., Highwood, E. J., Rosenberg, P. D., Trembath, J., Brooks, J. K. and co-authors. 2013. Optical properties of Saharan dust aerosol and contribution from the coarse mode as measured during the Fennec 2011 aircraft campaign. *Atmos. Chem. Phys.* **13**, 303–325.

Schell, B., Ackermann, I. J. and Hass, H. 2001. Modeling the formation of secondary organic aerosol within a comprehensive air quality model system. *J. Geophys. Res.* **106**, 28275–28293.

Schepanski, K., Tegen, I. and Macke, A. 2009b. Saharan dust transport and deposition towards the tropical northern Atlantic. *Atmos. Chem. Phys.* **9**, 1173–1189.

Schepanski, K., Tegen, I., Todd, M. C., Heinold, B., Bönisch, G. and co-authors. 2009a. Meteorological processes forcing Saharan dust emission inferred from MSG-SEVIRI observations of subdaily dust source activation and numerical models. *J. Geophys. Res. Atmos.* **114**, D10201.

Schladitz, A., Müller, T., Kaaden, N., Massling, A., Kandler, K. and co-authors. 2009. In situ measurements of optical properties at Tinfou (Morocco) during the Saharan Mineral Dust Experiment SAMUM 2006. *Tellus B*. **61**, 64–78.

Shao, Y. 2001. A model for mineral dust emission. *J. Geophys. Res. Atmos.* **106**, 20239–20254.

Shao, Y. 2004. Simplification of a dust emission scheme and comparison with data. *J. Geophys. Res. Atmos.* **109**, D10202.

Shao, Y. 2008. *Physics and Modelling of Wind Erosion*. Springer Verlag, Cologne, Germany.

Skamarock, W. C., Klemp, J. B., Dudhia, J., Gill, D. O., Barker, D. M. and co-authors. 2005. *A Description of the Advanced Research WRF Version 3*. Mesoscale and Microscale Meteorological Division, National Center for Atmospheric Research, Boulder, CO.

Sokolik, I. N. and Toon, O. B. 1999. Incorporation of mineralogical composition into models of the radiative properties of mineral aerosol from UV to IR wavelengths. *J. Geophys. Res. Atmos.* **104**, 9423–9444.

Solomos, S., Kallos, G., Mavromatidis, E. and Kushta, J. 2012. Density currents as a desert dust mobilization mechanism. *Atmos. Chem. Phys. Discuss.* **12**, 21579–21614.

Stockwell, W. R., Middleton, P., Chang, J. S. and Tang, X. 1990. The second generation regional acid deposition model chemical mechanism for regional air quality modelling. *J. Geophys. Res.* **95**, 16343–16367.

Sutton, L. J. 1925. Haboobs. *Q. J. Roy. Meteorol. Soc.* **51**, 25–30.

Takemi, T. and Seino, N. 2005. Dust storms and cyclone tracks over the arid regions in east Asia in spring. *J. Geophys. Res.* **110**, D18S11.

Tesche, M., Ansmann, A., Müller, D., Althausen, D., Mattis, I. N. A. and co-authors. 2009. Vertical profiling of Saharan dust with Raman lidars and airborne HSRL in southern Morocco during SAMUM. *Tellus B*. **61**, 144–164.

Todd, M. C., Washington, R., Raghavan, S., Lizcano, G. and Knippertz, P. 2008. Regional model simulations of the Bodélé low-level jet of Northern Chad during the Bodélé Dust Experiment (BoDEx 2005). *J. Clim.* **21**, 995–1012.

Varga, G. 2012. Spatio-temporal distribution of dust storms – a global coverage using NASA TOMS aerosol measurements. *Hungar. Geograph. Bull.* **61**, 275–298.

Wang, W., Bruyère, C., Duda, M., Dudhia, J., Gill, D. and co-authors. 2014. *Weather Research Forecasting ARW – Version 3 Modeling System User's Guide*. National Center for Atmospheric Research, Boulder.

Weinzierl, B., Petzold, A., Esselborn, M., Wirth, M., Rasp, K. and co-authors. 2009. Airborne measurements of dust layer properties, particle size distribution and mixing state of Saharan dust during SAMUM 2006. *Tellus B*. **61**, 96–117.

Wild, O., Zhu, X., Prather, M. J. and Fast, J. D. 2000. Accurate simulation of in- and below-cloud photolysis in tropospheric chemical models. *J. Atmos. Chem.* **37**, 245–282.

Yasui, M., Zhou, J., Liu, L., Itabe, T., Mizutani, K. and co-authors. 2005. Vertical profiles of Aeolian dust in a desert atmosphere observed using Lidar in Shapotou, China. *J. Meteorol. Soc. Jpn.* **83A**, 149–171.

Zender, C. S., Huisheng, B. and David, N. 2003b. Mineral Dust Entrainment and Deposition (DEAD) model: description and 1990s dust climatology. *J. Geophys. Res. Atmos.* **108**, 4416.

Zender, C. S., Newman, D. and Torres, O. 2003a. Spatial heterogeneity in Aeolian erodibility: uniform, topographic, geomorphic, and hydrologic hypotheses. *J. Geophys. Res. Atmos.* **108**, 4543.

Zhao, C., Chen, S., Leung, L. R., Qian, Y., Kok, J. F. and co-authors. 2013. Uncertainty in modelling dust mass balance and radiative forcing from size parameterization. *Atmos. Chem. Phys.* **13**, 10733–10753.

Zhao, C., Liu, X., Leung, L. R., Johnson, B., McFarlane, S. A. and co-authors. 2010. The spatial distribution of mineral dust and its shortwave radiative forcing over North Africa: modelling sensitivities to dust emissions and aerosol size treatments. *Atmos. Chem. Phys.* **10**, 8821–8838.